Biophysical Journal
Article

Biophysical Society

Charge and redox states modulate granulin—TDP-43 coacervation toward phase separation or aggregation

Anukool A. Bhopatkar,[1] Shailendra Dhakal,[1] Hannah G. Abernathy,[2] Sarah E. Morgan,[2] and Vijayaraghavan Rangachari[1,3,*]

[1]Department of Chemistry and Biochemistry, School of Mathematics and Natural Sciences, University of Southern Mississippi, Hattiesburg, Mississippi; [2]School of Polymer Science and Engineering, University of Southern Mississippi, Hattiesburg, Mississippi; and [3]Center for Molecular and Cellular Biosciences, University of Southern Mississippi, Hattiesburg, Mississippi

ABSTRACT Cytoplasmic inclusions containing aberrant proteolytic fragments of TDP-43 are associated with frontotemporal lobar degeneration (FTLD) and other related pathologies. In FTLD, TDP-43 is translocated into the cytoplasm and proteolytically cleaved to generate a prion-like domain (PrLD) containing C-terminal fragments (C25 and C35) that form toxic inclusions. Under stress, TDP-43 partitions into membraneless organelles called stress granules (SGs) by coacervating with RNA and other proteins. To study the factors that influence the dynamics between these cytoplasmic foci, we investigated the effects of cysteine-rich granulins (GRNs 1–7), which are the proteolytic products of progranulin, a protein implicated in FTLD, on TDP-43. We show that extracellular GRNs, typically generated during inflammation, internalize and colocalize with PrLD as puncta in the cytoplasm of neuroblastoma cells but show less likelihood of their presence in SGs. In addition, we show GRNs and PrLD coacervate to undergo liquid-liquid phase separation (LLPS) or form gel- or solid-like aggregates. Using charge patterning and conserved cysteines among the wild-type GRNs as guides, along with specifically engineered mutants, we discover that the negative charges on GRNs drive LLPS while the positive charges and the redox state of cysteines modulate these phase transitions. Furthermore, RNA and GRNs compete and expel one another from PrLD condensates, providing a basis for GRN's absence in SGs. Together, the results help uncover potential modulatory mechanisms by which extracellular GRNs, formed during chronic inflam-matory conditions, could internalize and modulate cytoplasmic TDP-43 inclusions in proteinopathies.

SIGNIFICANCE TDP-43 has emerged as a key player in the formation of stress granules and amyloids. To gain insights into the factors that influence the dynamics between these cytoplasmic foci, we investigated the effects of cystine-rich granulins (GRNs) on TDP-43, which are proteolytic fragments of progranulin, a protein implicated in frontotemporal lobar degeneration. We discover that GRN s promote solid-like aggregates or liquid-like droplets of TDP-43 depending on the charge distributions and redox state of cysteines on GRNs. Using wild type and specifically engineered mutants, we uncover potential modulatory mechanisms of GRNs on TDP-43 proteinopathies and stress response.

INTRODUCTION

Frontotemporal lobar degeneration (FTLD) is a progressive neurodegenerative disease that affects the frontal and temporal lobes of patients predominantly 45–65 years of age (1). The neuronal atrophy observed in these patients is associated with language impairments accompanied by behavioral and personality changes (2,3). Based on histopathological signatures, FTLD is subclassified into FTLD-TDP, FTLD-Tau, and FTLD-FUS (rare) (1,4,5). Nearly half of FTLD patients show the presence of neuronal and glial cytoplasmic inclusions of TAR DNA binding protein-43 (TDP-43) (5), making FTLD-TDP a predominant category of the disease. Furthermore, 95% of sporadic amyotrophic lateral sclerosis (ALS) patients also show TDP-43 inclusions besides sharing common genetic etiologies with FTLD, making FTLD-TDP and ALS part of a clinicopathological continuum (5). Etiology of familial FTLD is associated with mutations in microtubule-associated protein tau (MAPT) for FTLD-Tau, and

Submitted November 5, 2021, and accepted for publication April 27, 2022.

*Correspondence: Vijay.rangachari@usm.edu

Present address: Anukool A. Bhopatkar, Mitchell Center for Neurodegenerative Disorders, University of Texas Medical Branch, 301 University Blvd, Route 1045, Galveston, TX 77555, USA

Editor: Jane Dyson.

https://doi.org/10.1016/j.bpj.2022.04.034

2022 Biophysical Society.

those in progranulin (GRN), TDP-43 (TARDBP), fused in sarcoma (FUS), and hexanucleotide repeat expansion in C9orf72 (C9orf72), for FTLD-TDP (2,4,6).

TDP-43 is a 43-kDa protein that contains an N-terminal domain, two RNA recognition motifs (RRMs), and a prion-like disordered, C-terminal domain enriched with low-complexity sequences (PrLD) (4,7). Localized in the nucleus, TDP-43 is involved in a wide range of functions, including transcriptional regulation, RNA metabolism, and splicing (8–10). Under cellular stress such as heat shock, oxidative insults, inflammation (11,12), or nutrient starvation (12), TDP-43 coacervates with mRNA and other proteins to undergo liquid-liquid phase separation (LLPS) and partitions into membraneless organelles called stress granules (SGs) (11,13). SGs are reversible cytoplasmic membraneless organelles formed in response to cellular stress to sequester and prevent mRNA transcripts from degradation or translation (14–16). In pathological conditions, TDP-43 is translocated to the cytoplasm where it undergoes aberrant proteolytic cleavage to generate several C-terminal fragments (CTFs) of varying sizes including C35 (35 kDa), C25 (25 kDa), and C17 (17 kDa), with the former two being the most abundant of them (17–20). These fragments are also known to be formed by alternative splicing to varying degrees (21). Importantly, TDP-43 CTFs undergo aggregation to form toxic, insoluble inclusions in the cytoplasm that are the pathological hallmarks of ALS and FTLD patients (19,22). Despite the conspicuity of the TDP-43 CTF aggregates in patients, factors responsible for their biogenesis and subsequent roles in pathology remain poorly understood. Similarly, while the formation and functions of biomolecular condensates is well established for TDP-43 and other members of SGs, such as hnRNP1 (23,24), FUS (23,25), and TIA1 (23,26), the link between SGs and amyloid formation remains ambiguous, but one that could be key in neurodegenerative pathologies.

Another key protein implicated in FTLD is a 68.5-kDa secreted protein called progranulin (PGRN). The protein possesses pleiotropic functions including wound healing, tumorigenesis (27), and immunomodulation (28). In neurons, PGRN is involved in functions such as lysosomal homeostasis, cell survival, and differentiation (29–35), and has gained significant attention due to its link to neurodegenerative pathologies, especially FTLD. About 30%–50% of FTLD-TDP cases are of a heritable type, with mutations in GRN underlying a majority of them (36,37). The autosomal dominant heterozygous GRN mutations result in haploinsufficiency of the protein, which led to the conclusion that PGRN plays a neuroprotective role (38–40), while homozygous GRN mutations lead to neuronal ceroid lipofuscinosis (NCL), a lysosomal disease (39,41). Other than the genetic connection and haploinsufficiency, the precise mechanism by which PGRN may influence FTLD remains unknown. In this context, the cysteine-rich, 6-kDa modules called GRNs (GRNs 1–7), which are the proteolytic products of PGRN (42), have been of great interest to us for their potential roles in FTLD and other related pathologies. It is now known that extracellular PGRN is endocytosed into the lysosome via a sortilin-mediated pathway to be processed by cathepsins into GRNs (43), which are thus speculated to possess lysosomal functions (44,45). GRNs also function in a plethora of roles in normal cell biology (29,46,47) but possess opposing inflammatory properties to PGRN; while PGRN is anti-inflammatory, GRNs show pro-inflammatory properties (42). During inflammation, PGRN secreted from activated microglia and astrocytes undergoes extracellular proteolysis by neutrophil elastases and other proteases to generate GRNs (48). The fate of the extracellular GRNs on neuronal function and dysfunction remains undetermined and we hypothesize that they are taken up by neurons where they interact with modulate TDP-43 assemblies. Some support for this idea came from a report from Salazar and coworkers, who showed that specific GRNs affected TDP-43 toxicity and behavior functions in a Caenorhabditis elegans model (49). We also demonstrated that GRNs 3 and 5 interact with and modulate the aggregation and phase behavior of TDP-43 PrLD in vitro (50). Furthermore, GRN immunopositivity observed in several regions of the brain in post-mortem Alzheimer's disease and FTLD-TDP patients potentiates the significance of GRNs in pathology (51). Importantly, acute inflammation such as traumatic brain injury (TBI) has been shown to induce mislocalization, proteolysis, and aggregation of TDP-43 in humans, mice, and cell culture (52,53), increasing the likelihood of its interaction with the pro-inflammatory GRNs.

Here, we delve deep into understanding the molecular factors that govern the interactions between GRNs and TPD-43 PrLD (termed PrLD hereafter). These investigations were motivated by the following three broad questions: 1) do extracellular GRNs generated during inflammation from PGRN internalize in neurons? 2) What are the molecular determinants on GRNs that determine their interactions with PrLD. 3) How do GRNs modulate PrLD phase transitions? Our results show that extracellular GRN-2, -3, and -5 internalize and colocalize with PrLD in the cytosol of neuroblastoma cells but do not partition into the SGs formed under stress with PrLD. In vitro biophysical experiments suggest that GRN-2 undergoes coacervation with PrLD to form liquid droplets in the oxidized state but promotes gelated/insoluble aggregates in the reduced state. With time, the droplets transform into a gelated state that shows amyloid-like characteristics. Based on the empirical results derived from GRNs along with designed mutations and chemical modifications, we determine that the coacervation of GRN and PrLD forming liquid droplets is predominantly driven by the negatively charged residues on GRNs, while the increase in the number of positively charged residues promotes distorted gel-like droplets and aggregation. Furthermore, we determine that the redox state of cysteines in GRNs is a key modulator of phase transitions by fine-tuning LLPS or aggregation of PrLD when electrostatic charges on GRNs are nearly counterbalanced. Additionally, we show that RNA expels GRNs from

the PrLD droplets, which provides a possible reason for not observing GRNs within the SGs.

MATERIALS AND METHODS

Recombinant expression and purification of proteins

GRNs

GRNs (GRN-2, GRN-2(þ/), GRN-2(C/A), GRN-2DAro, GRN-3, GRN-5, and GRN-7) were recombinantly expressed and purified as previously described, where GRN-3 was expressed in Escherichia coli SHuffle cells (New England Biolabs), while other GRNs were expressed in Origami 2 DE3 cells (Invitrogen) (50). Briefly, GRNs were expressed as fusion constructs containing an N-terminal thioredoxin-A and His_6 tag with an intervening thrombin cleavage site. The fusion constructs were purified using immobilized-nickel affinity chromatography. The purified construct was cleaved using restriction grade bovine thrombin (BioPharm Laboratories) at 3 units/ 1 mg of protein for 24 h at room temperature to separate the fused tags. For GRN-2DAro, purification protocol was modified to minimize thiol oxidation; typically, buffers were degassed prior to use and the purification was carried out at 4C to reduce oxygen solubility. After nickell affinity, all samples was fractionated using semipreparative Jupiter 5 mm-10 250 mm C18 reverse-phase high-performance liquid chromatography (HPLC) column (Phenomenex) using a gradient elution of 60%–80% acetonitrile containing 0.1% TFA. Fractionated protein was lyophilized and stored at 20C. For the generation of 2-alkylated GRN-2 (i.e., GRN-2 with two free thiols that are alkylated), the protein was incubated with 10 molar excess of iodoacetamide post thrombin cleavage for a period of 24 h at room temperature. Protein was then fractionated using reverse-phase HPLC as mentioned before. For the generation of 12-alkylated GRN-2 (i.e., GRN-2 with all 12 thiols alkylated), the protein was incubated with 12molar excess of tris(2-carboxyethyl)phosphine (TCEP) post-thrombin cleavage for a period of 12 h at room temperature followed by incubation with 10 molar excess of iodoacetamide for 24 h at room temperature. Protein was then fractionated using reverse-phase HPLC as before. The purity of protein was confirmed using matrix-assisted laser desorption-ionization time-of-flight mass spectroscopy (MALDI-ToF MS).

TDP-43 PrLD

PrLD was expressed and purified as described previously (50). The plasmid for TDP-43 PrLD was a gift from Dr. Nicolas Fawzi at Brown University (Addgene plasmid 98669, RRID: Addgene 98669). Briefly, the protein was expressed as a fusion construct with an N-terminal His_6 tag followed by tobacco etch virus (TEV) protease cleavage site in E. coli BL21 DE3 Star cells (Invitrogen). The fusion construct was purified using immobilized-nickel affinity chromatography with suitable modifications of the protocol described in the report by Conicella et al. (54). Purified protein construct (with the intact N-terminal His_6) was concentrated using Amicon Ultra-Centrifugal units (Millipore) and flash frozen for storage at 80C or used immediately for experiments.

Preparation of proteins and RNA

GRNs

Lyophilized protein was resuspended in required buffer (20 mM MES, pH 6.0, or 20 mM ammonium formate, pH 4.5) and the concentration was estimated spectrophotometrically at 280 nm with extinction coefficients of 6250 M^1 cm^1 for GRN-2, GRN-2(þ/), and GRN-3; 5500 M^1 cm^1 for GRN-2(C/A); 7740 M^1 cm^1 for GRN-5; or at 215 nm for GRN-2DAro with an extinction coefficient of 90,000 M^1 cm^1. The number of free thiols within GRNs was estimated using Ellman's assay and by alkylation with iodoacetamide, as described previously (55). The reduced forms of GRN were generated by incubating the freshly purified proteins with 12 molar excess of TCEP at room temperature for 2–4 h or at 4C for 12 h. Fluorescent labeling of GRNs was performed using HiLyte Fluor 405 succinimidyl ester (AnaSpec) or HiLyte Fluor 647 succinimidyl ester for fluorescence recovery after photobleaching (FRAP) studies on GRNs. Proteins were incubated with 3 molar excess of dyes at 4C for 12 h and excess dye was excluded using clarion MINI Spin Columns, Desalt S-25 (Sorbent Technologies).

PrLD

Before the experiments, the protein was buffer exchanged into 20 mM MES, pH 6.0, or 20 mM ammonium formate, pH 4.5, using PD SpinTrap G-25 desalting columns (Cytiva) and the concentration was estimated using an extinction coefficient of 19,480 M^1 cm^1 at 280 nm. Aliquots of the purified protein were either used immediately after purification or flash frozen and stored 80C for later use. The frozen proteins were used within a week of purification. Fluorescent labeling of PrLD was performed using HiLyte Fluor 647 succinimidyl ester (AnaSpec) using a similar protocol as described above for GRNs.

RNA

Lyophilized poly-A (Sigma Aldrich) was resuspended in deionized, sterilized water at a concentration of 1 mg/mL. The concentration of the stock was estimated by considering a value of 1 absorbance unit to correspond to 40 mg of RNA. The prepared stock was flash frozen and stored at 80C. Aliquots of prepared stock were thawed and used immediately for experiments.

Cell growth, transfection, and colocalization analysis

SH-SY5Y neuroblastoma cells (ATCC, Manassas, VA) were grown in DMEM:F12 (1:1) medium containing 10% FBS (Gibco, Thermo Scientific) and were maintained in humidified condition at 37C with 5.5% CO_2. Cells were seeded 24 h before transfection. Cells were transfected with PrLD-SBFP2 or wtTDP43tdTomato plasmid using the TransIT-X2 dynamic delivery system, Mirius (1:3), in Opti-MEM media (Thermo Scientific). Cell confluency was allowed to reach 70%–80% prior to transfection. After 24 h, cells were gently washed twice with fresh medium and 500 nM fluorescently labeled recombinant GRNs were added. Cells were incubated with GRN-containing medium for 24 h. Following this, medium was replaced with GRN-devoid medium and cells were incubated for a further 1 h. For inducing stress, sodium arsenite was added at a final concentration of 0.5 mM and incubated for 30 min. Cells were stained with nuclear (NucSpot Live 650, Biotium) or lysosomal (Lysoview 650, Biotium) markers prior to imaging at 40 magnification using Leica STELLARIS-DMI8 microscope. For colocalization analysis of GRNs and PrLD, the respective channels for PrLD and GRNs were converted to 16-bit grayscale format and region of interest was selected. Images were processed using Coloc2 parameter in Fiji ImageJ software using Costes threshold regression, and Manders' tM1 values were reported. All the confocal images were processed using Adobe illustrator, and data were processed using OriginPro 8.5 software. FRAP analysis was done on puncta under stress conditions and each datum was normalized against the background fluorescence as minimum and intensity within the puncta as maximum. This ensured that every FRAP datum is comparable without variations in expression levels affecting such analysis.

Immunofluorescence

For the immunofluorescence experiment, cells were plated on to a 12-well plate, 24 h prior to transfection with PrLD-SBFP2 as described above. Af-ter incubating with fluorophore-labeled GRNs for 24 h, medium was

replaced, and the experiments were carried out in both stress and non-stress conditions. For induction of stress, 0.5 mM sodium arsenite was added to the medium and incubated for 30 min followed by washing with PBS buffer. Cells were fixed in 4% paraformaldehyde for 20 min and washed twice with PBS. These were further permeabilized with 0.2% Triton X-100 in PBS for 20 min. Cells were washed and blocked using 3% BSA for 2 h. Cells were then incubated with anti-TIA1 primary antibodies (Cell Signaling Technology, TIAR XP rabbit monoclonal antibody #8509) and anti-rabbit secondary antibodies (Cell Signaling Technology, Alexa Flour 488 conjugate #4412) and imaged following the addition of anti-fade mounting medium at 40 magnification on a Leica STELLARIS-DMI8 microscope.

DIC microscopy and FRAP analysis

Differential interference contrast (DIC) and fluorescence microscopy images were acquired on a Leica STELLARIS-DMI8 microscope. The assays were performed in an optical-bottom 96-well plate (Thermo) and were covered with an optically clear sealing tape (Nunc, Thermo Scientific) to prevent evaporation. The reactions were initiated at room temperature and were visualized within 10–15 min of mixing. Brightfield and fluorescence images were acquired at a magnification of 40 or 63 with an oil immersion objective. For the ternary interactions between GRN-2, PrLD, and RNA, heterotypic condensates of PrLD with GRN-2 were generated, followed by titration with desired volumes of the RNA stock. Images were acquired after an equilibration time of 10–15 min after each titration. The RNA stocks were prepared at a high initial concentration to minimize dilution effects upon titration. For fluorescence imaging and FRAP studies, samples were prepared by mixing the required concentration of proteins in an optical-bottom 96-well plate in the presence of 1% fluorophore-labeled proteins. For FRAP studies, fluorescence intensities were acquired pre- (2 s) and post bleach (30 s) at an interval of 68 ms. Bleaching period was varied from 10 to 20 s with a laser intensity of 100%, while the laser intensity for imaging was set at 2%–10%. The online white and diode 405 laser was utilized in all imaging studies. The fluorescence recovery data were processed using Leica LasX program and Origin 8.5 graphing soft-ware. The recovery curves of at least three independent and individual samples were averaged and normalized with respect to the pre-bleach fluorescence intensities. To discern the rate constants of recovery kinetics post bleach, the initial-rate method was utilized (56,57). Briefly, a period of fluorescence recovery 1 s post bleach was evaluated via a linear fit with the slope of the line providing a rate constant, k (s^1). Rate con-stants were obtained by evaluating three FRAP recovery curves for each sample. For kinetic experiments, FRAP analysis was performed on samples at initial time (0 h) and after incubation of 24 h at 37C under quiescent conditions.

Post image analysis

Droplet area distribution

Area of the droplets formed within various samples was ascertained using the ImageJ program. Briefly, the fluorescence images acquired for the respective samples were subjected to color thresholding at default values in the program. Areas of droplets within the threshold images were then extracted using the included particle analyzer tool of the program. A lower limit of either 50 or 200 ($pixel^2$) (depending on image magnification) was placed on area of particles to be analyzed so as to exclude detection of small artifacts. Areas obtained in $pixel^2$ were converted into mm^2 by correlating with the scale bar. The obtained data were then plotted as a histogram overlayed with normal distribution curve using Origin 8.5. A set of 100 droplets were enumerated from at least two different fields for each sample.

Fluorescence intensity profiles

To qualitatively ascertain the displacement of GRN-2 from condensates upon titration with RNA, the fluorescence intensity profiles of the fluorophore-labeled proteins from the images of the respective samples were determined using the ImageJ program. Intensity profiles were obtained by mapping a line segment across the width of a droplet and extracting the intensities of the fluorophores (HiLyte 405 for GRN-2 and HiLyte 647 for PrLD) using the plot-profile tool. The plot-profile tool provides in-tensity values within an arbitrary window of 0–80 units, with highly fluo-rescent samples being cut off at the upper limit. The fluorophore intensities obtained across a pixel scale were then converted into mm using the scale bar. The fluorescence intensity profile was extracted from indi-vidual droplets for each sample but are representative of the entire field containing at least 20 different such droplets.

Turbidimetric assays

Turbidity measurements were performed on a BioTek Synergy H1 microplate reader. Reactions were initiated and allowed to equilibrate at room temperature for 3–10 min before each measurement. For titration experiments with GRNs, 1,6-hexanediol (HD), NaCl, or RNA, stocks were prepared at high concentrations to minimize dilution of samples.

Establishment of phase boundaries

For establishment of phase diagrams, a boundary value of 0.140 optical density 600 (OD_{600}) was set and readings above it were considered to undergo phase transition. A temperature-dependent phase diagram was established by equilibrating samples at respective temperature (4C, room temperature) for 15 min, while temperatures above 30C were achieved using the internal temperature control capability of the plate reader. Data processing was performed on Origin 8.5. At least three independent datasets were averaged.

Aggregation assay

To monitor the amyloid formation of PrLD in the presence of GRN-2 or rGRN-2, thioflavin-T (ThT) fluorescence assays were performed on a BioTek Synergy H1 microplate reader. The aggregation of PrLD was monitored in the presence of different molar concentrations of GRN-2 or rGRN-2 in separate reactions in the presence of 15 mM ThT dye. The reactions were monitored for a period of 24 h under quiescent conditions at 37C and are representative of three independent datasets.

MALDI-ToF MS

For confirming the purity and for characterization of proteins used, MALDI-ToF MS was performed on a Bruker Daltonics Microflex LT/SH TOF MS system. Prepared samples were spotted onto a Bruker MSP 96 MicroScout Target microchip with a 1:1 ratio of sample:sinapinic acid matrix in saturated acetonitrile and water. Instrument calibration was performed using Bruker Protein Calibration Standard I (Bruker Daltonics). Alkylation assays of GRNs using iodoacetamide were performed as described (58).

Atomic force microscopy

Atomic force microscopy (AFM) images were obtained following a previously published method (59,60). Briefly, mica was cleaved using tape then attached to a magnet. The mica was then treated with 150 mL of 3-aminopropyltriethoxysilane (APTES) solution (500 mL of APTES in 50 mL of 1 mM acetic acid) for 30 min. The APTES solution was then dec-anted off and the mica substrate was rinsed three times with nanopure H_2O, dried with N_2, and stored for an hour. A volume of 70 mL of the sample

solution was deposited onto the mica surface and allowed to absorb for 30 min. The sample solution was then decanted from the mica surface and washed with 150 mL of nanopure H_2O three times, dried with N_2, and stored in a desiccator until imaging. AFM analysis was performed using a Dimension Icon atomic force microscope (Bruker) in PeakForce Tapping mode. AFM scanning was performed using NanoScope 8.15 software and the images were analyzed in NanoScope Analysis 3.0 software. Measurements were performed under ambient environmental conditions at a constant scan rate of 1 Hz in tapping mode using a sharp silicon nitride cantilever (RTESPA; nominal tip radius of 8 nm; nominal resonance frequency of 300 kHz; nominal spring constant of 40 N/m) and a standard probe holder with 512 512 data point resolution. Multiple areas of the mica surface were analyzed, height and phase images were obtained simultaneously, and representative images are reported.

In silico analysis and figure preparation

Redox-dependent disorder scores for individual proteins were obtained using IUPred2A platform (61). Specifically, the FASTA sequence of each protein was evaluated by coupling the IUPred2 long disorder algorithm with a redox-state tool (62). The hydropathy indices for GRNs were obtained using the CIDER platform (63). The net charge and isoelectric points (pIs) of the individual proteins were determined using the SnapGene program. The obtained figures were processed using the Adobe Illustrator CC suite and Affinity Designer.

RESULTS

Extracellular GRN-2 colocalizes with TDP-43 PrLD in the cytoplasm but not in SGs

Unlike GRNs generated in the lysosomes, the fate of those formed extracellularly, especially during inflammation, remains unclear, although transport to the cytosol has remained a possibility (47,51,64). The ambiguity surrounding the precise localization of GRNs in pathophysiology has also hindered understanding of their cellular functions (45,65). We hypothesize that extracellular GRNs are internalized in the neuronal cytoplasm and potentially interact with proteolytic fragments of TDP-43, modulating the latter in ALS and FTLD pathologies. To recapitulate this scenario, we utilized a simple pulse-chase assay with fluorophore-labeled GRNs (45). In this assay, SH-SY5Y cells transiently expressing a blue fluorescent protein-tagged PrLD construct (PrLD-SBFP2) were pulsed with medium containing 500 nM HiLyte532-labeled GRN-2 after 24 h (post transfection), and then chased using medium for an additional hour (see section "materials and methods"). The cells were then imaged under non-stress and stress (with $NaAsO_2$) conditions (Fig. 1). Under non-stress conditions, the transfected PrLD was observed in both the nucleus and cytoplasm (top panels, Fig. 1 a). Pulsing with GRN-2 showed internalization and colocalization with PrLD outside the nucleus (arrow, middle panels, Fig. 1 a). To see whether the colocalization was within or outside the lysosomes, as GRNs are known to be transported to lysosomes, the cells were observed using a lysosomal marker, which clearly indicted GRN-PrLD puncta outside the lysosomes (arrow, bottom panels, Fig. 1 a). Not surprisingly, some GRN-2 was also found to be localized within the lysosomes (yellow puncta, bottom panels, Fig. 1 a). FRAP of the cytoplasmic GRN-PrLD puncta showed no recovery of PrLD, suggesting that they are gel-like or solid-like aggregates (green, top panel, Fig. 1 c). In parallel, the samples were also immunodetected in the presence of TIA1 antibody, a key SG marker (66). In the non-stress conditions, TIA1 was located in the nucleus, while PrLD was dispersed throughout the cell (Fig. S1 a). TIA-1 was absent from the colocalized PrLD and GRN-2 puncta as would be expected under non-stress conditions (no stress, Fig. S1 d). Under stress conditions induced by sodium arsenite, the transfected PrLD showed puncta outside the nucleus (arrow, top panels, Fig. 1 b), consistent with SG formation (11,14). Surprisingly, the fluidity of SGs observed by FRAP showed no recovery (orange, top panel, Fig. 1 c), although widely varying photobleaching recovery rates for SGs have been reported in cellular models (67–69). Nevertheless, PrLD's presence in SGs was confirmed by the colocalization of PrLD with TIA1 (cyan, Fig. S1 b) with a Meander's tM1 value of 0.59 (Fig. S1 c). Pulsing GRN-2 onto these cells under stress showed colocalization of both the proteins as puncta in the cytoplasm and outside the lysosomes, similar to those observed under non-stress conditions (arrows, middle and bottom panels, Fig. 1 b). Here again, the colocalized puncta did not show fluorescence recovery (green, bottom panel, Fig. 1 c). Furthermore, in absence of stress, GRN-2 did not show colocalization with TIA1 and PrLD, suggesting that GRN-2 was not partitioned into the SGs (Fig. S1 d). In addition, two other GRNs known to modulate PrLD's phase transitions (50), GRN-3 and -5, also did not colocalize with TIA1 under stress conditions, but colocalized with PrLD under both non-stress and stress conditions (Fig. S1 d and e). Importantly, under stress, a three-way colocalization involving PrLD, GRN-2, and TIA1 was not observed. The colocalization of GRN-2 and PrLD was statistically significant, with 73% of the internalized GRN-2 found to be colocalized with PrLD under stress and 68% under homeostatic conditions (Fig. 1 d). Finally, gelated material-like properties of PrLD SGs implied by the lack of fluorescence recovery could be attributed to the absence of other domains in TDP-43. To see if this is the case, SH-SY5Y cells were transfected with the full-length wild-type TDP-43 (wtTDP43tdTomato) as a control (Fig. S2), which showed the FRAP recovery for SGs under stress conditions (Fig. S2 b). This possibly suggests that SG assemblies containing the truncated PrLD construct, and therefore other truncated CTFs of TDP-43 (C25 and C35), may indeed possess solid- or gel-like characteristics. However, caution needs to be exercised as an FRAP recovery alone is not an indicator of SGs, as mentioned above. Taken together, the data establish that extracellular GRN-2

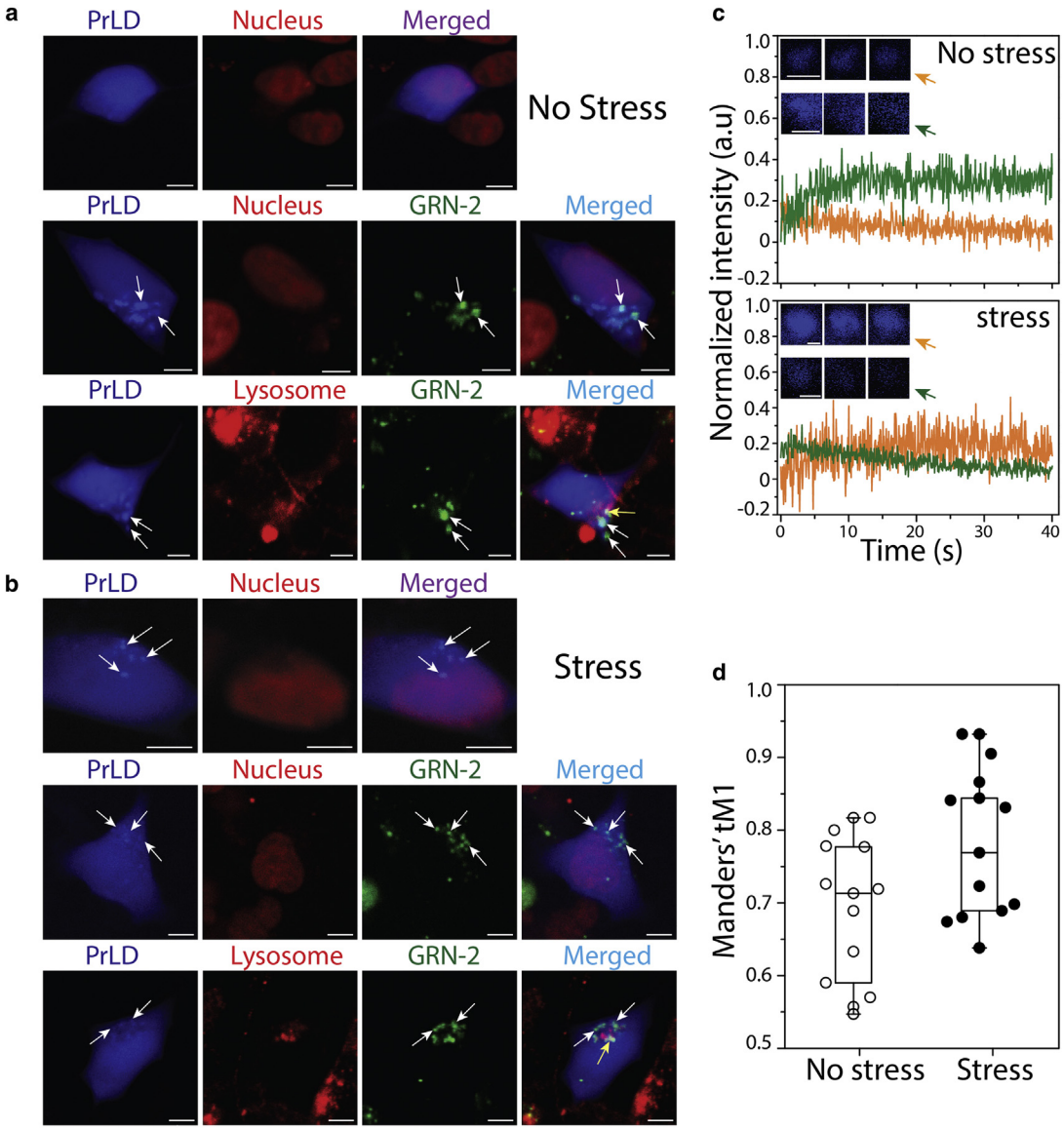

FIGURE 1 Cytoplasmic colocalization of GRN-2 and PrLD. Confocal microscopy images of live SH-SY5Ycells under homeostatic or stress conditions. (a) Blue fluorescent protein-tagged PrLD (PrLD-SBFP2) transiently expressed in SH-SY5Y cells alone and in the presence of HiLyte-532-labeled GRN-2 under non-stress conditions, and (b) the same reactions under stress induced by sodium arsenite. White arrows indicate colocalized GRN-2 and PrLD puncta in the cytoplasm, while yellow arrows represent colocalization of GRN-2 in lysosomes (scale bar represents 5 mm). Visualization of nucleus and lysosomes was done by staining with NucSpot Live 650 and Lysoview 650 respectively (c) Normalized intensities of fluorescence recovery after photobleaching (FRAP) for puncta of PrLD alone (orange) or colocalized PrLD-GRN-2 (green) in under non-stress (top) or stress (top) conditions. Inset: representative pre-bleach, post-bleach, and recovery intensities of the puncta. At least three different puncta were bleached. (d) Whiskers plot of Manders' tM1 calculated for the co-localization of GRN-2 with PrLD using Fiji ImageJ software. Each data point represents the colocalization score of an independent cell (n ¼ 14). To see this figure in color, go online.

internalizes and colocalizes with PrLD in the cytoplasm but is not present within the SGs.

GRN-2 modulates the phase transitions of PrLD in vitro

The observation of cytoplasmic puncta of colocalized PrLD and GRN-2 decoupled from SGs prompted us to investigate their interactions in greater detail. TDP-43 is known to undergo dynamic phase transitions depending on the cellular conditions to form either liquid condensates or solid aggregates (70–72). Understanding the molecular grammar of protein LLPS has revealed that weak, multivalent interactions between "stickers" involving electrostatics, p-p interactions (between tyrosines), or cation-p interactions (between aromatic residues and arginines and lysines) and separated by scaffolds called spacers are the main driving forces of condensate formation (24,73–75). Disordered

proteins enriched in one kind of charge will repel one another, preventing self-coacervation but counter interacting charges would minimize repulsion and promote LLPS (76). These interactions are also observed to be the driving forces behind the self-coacervation and complex (with RNA) coacervation of TDP-43 (54,77–80). However, the molecular determinants of heterotypic phase transitions of TDP-43 involving ligands vary depending on the partners and are still being discerned (78). Despite the lack of a canonical RNA-binding domain, TDP-43 PrLD undergoes coacervation with RNA, which illustrates the prominence of the aforementioned interactions in phase separation (50,54,81). However, the phase transitions are dictated by the balance between weak, multivalent interactions that drive LLPS, and strong, high-affinity interactions that mediate gelation or solid-like phase transition often observed among amyloid proteins (78). Our earlier investigations into the interactions of PrLD with GRN-3 and GRN-5 showed that GRN-3 induces aggregation in both oxidizing and reducing conditions, while GRN-5 undergoes LLPS by complex coacervation with PrLD (50). We conjecture that the disparity in the behavior of GRNs is due to the high net negative charge on GRN-5 (–6; six – and no þ charges; Fig. 2 d) as opposed to GRN-3 (–2; seven – and two þ charges; Fig. 2 c) that interact with PrLD (Fig. 2 a). It is also likely that the lack of positive charges on GRN-5 plays a role in its ability to phase separate PrLD. Here, we extended these investigations to uncouple the sequence determinants on GRNs to phase separate or co-aggregate with PrLD by investigating GRN-2 and specifically designed mutants. All three GRNs, GRN-2, -3, and -5, possess a similar number of negatively charged acidic residues (seven, six, and six respectively; Fig. 2 b–d) but vary in the number of positively charged basic residues (two, four, and zero, respectively; Fig. 2 b–d), making GRN-2 ideal to investigate. The presence of structural disorder in proteins is also known to be an implicit contributor to LLPS (82–86); PrLD is largely a disordered region of TDP-43, while GRN-2 is also predicted to be disordered in the fully reduced state by IUPred2A (Fig. S3 a and b) (61,62). This prediction was confirmed by biophysical characterization of GRN-2, which revealed a structure dominated by random coils in both redox forms (Fig. S4 a), similar to GRN-3 and -5 (50) (Figs. S3 c, d, and S4 e).

To probe the ability of GRN-2 in both redox forms to modulate phase transitions of PrLD, 40 mM GRN-2 (oxidized form) or rGRN-2 (fully reduced form) were mixed with 20 mM PrLD buffered in 20 mM MES, pH 6.0, and the samples were visualized by DIC microscopy (Fig. 3 a–d). Immediately upon co-incubation of GRN-2 and PrLD, the sample phase separated into liquid droplets ranging between 2 and 12 mm diameter (Fig. 3 a). The droplets also showed classic wetting behavior suggestive of their liquid-like characteristics (arrow, Fig. 3 b). The colocalization of proteins within the droplets was confirmed using orthogonal fluorophores, HiLyte405 (blue) and HiLyte647 (red) for GRN-2

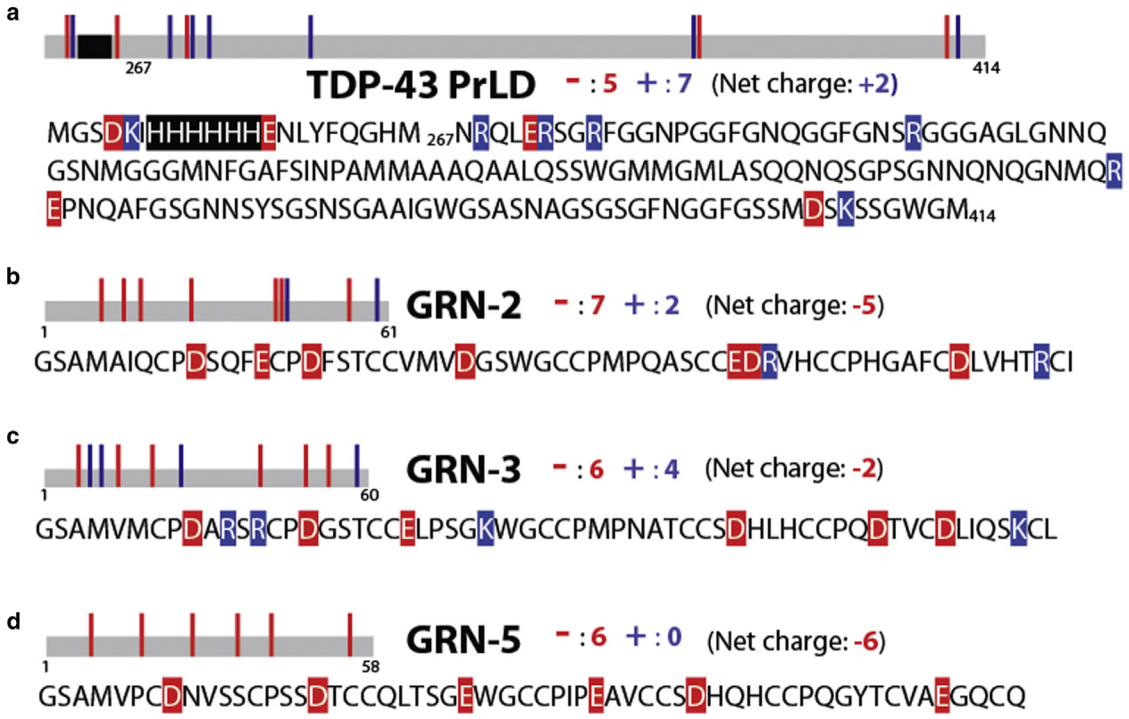

FIGURE 2 Sequences of granulins (GRNs) and TDP-43 under investigation. (a) TDP-43 PrLD construct (residues 267–414) along with a hexa-histidine tag (highlighted) used in the study. (b–d) Sequences of GRN-2 (b), GRN-3 (c), and GRN-5 (d). Sequences of proteins are annotated with acidic (red) and basic (blue) residues, along with the net charges on the respective proteins at neutral pH. To see this figure in color, go online.

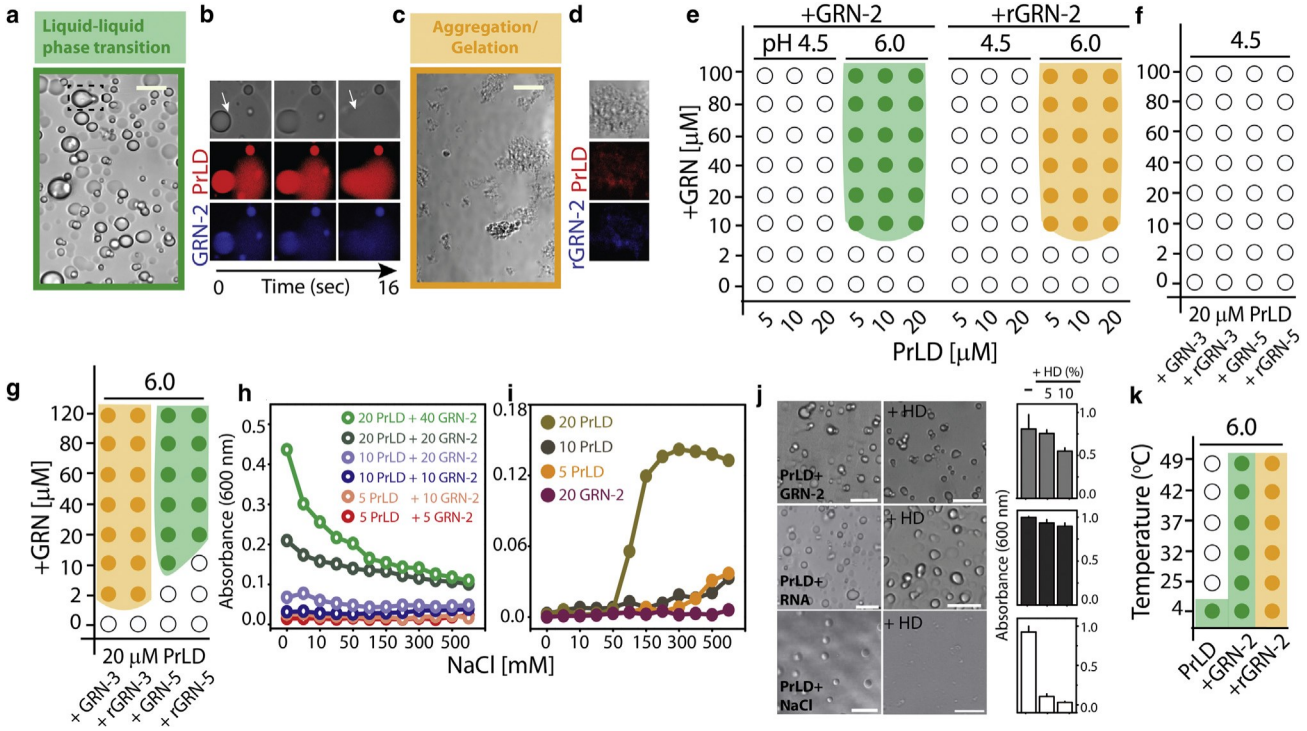

FIGURE 3 Phase transitions involved in GRN-TDP-43 PrLD interactions. (a–d). DIC microscopy images of a mixture containing 20 mM PrLD with 40 mM fully oxidized GRN-2 (a and b) or reduced rGRN-2 (c and d) in 20 mM MES, pH 6.0. GRN-2 undergoes LLPS with PrLD (highlighted with green box), which shows the coalescence of droplets (a, dashed box), while rGRN-2 undergoes gelation/aggregation (saffron box). GRN-2 or rGRN-2 labeled with HiLyte 405 (blue) and PrLD with HiLyte 647(red) were visualized using confocal fluorescence microscopy, which shows fusion of droplets for GRN-2 (white arrow; b) and deposition of solid aggregates for rGRN-2 (d). (e) Phase diagram for GRN-2 or rGRN-2 with PrLD generated by varying the pH (buffered with 20 mM ammonium formate at pH 4.5 or 20 mM MES at pH 6.0) and concentrations of the respective proteins. (g and h) Phase diagram for varying con-centrations of GRN-3 and GRN-5 with 20 mM PrLD at pH 4.5 (f) and pH 6.0 (g). (h) Turbidity measurements monitored at 600 nm for PrLD-GRN-2 re-actions with different stoichiometries in increasing NaCl concentrations (1–750 mM). (i) Turbidites of the control reactions for samples in (h). (j) A mixture containing 40 mM GRN-2 with 20 mM PrLD was treated with 5% and 10% 1,6-hexanediol (HD) to monitor its effect on the LLPS of the proteins, which was quantified using OD_{600} values pre- and post HD treatment. Similar treatment was performed for condensates of 20 mM PrLD with either RNA (75 mg/mL) or NaCl (300 mM). The turbidity values were normalized with respect to their values pre-HD treatment (n ¼ 3). The concentrations of components used in this assay (GRN-2, RNA, PrLD, and NaCl) were carefully chosen to be well within the demixing boundary conditions of the individual phase transitions. (k) The turbidity of 20 mM PrLD alone, or in presence of 40 mM GRN-2 or rGRN-2 measured as a function of temperature. The phase boundaries were established by considering an OD_{600} value of 0.14 as a cutoff for phase transitions. Scale bar represents 10 mm. For (e)–(k), three independent data points (n ¼ 3) were averaged. To see this figure in color, go online.

and PrLD, respectively, and their liquid-like properties by coalescence and fusion of droplets (Fig. 3 b). In stark contrast, samples containing rGRN-2 and PrLD showed the formation of solid insoluble aggregates (Fig. 3 c), which also involved colocalization of both proteins (Fig. 3 d). These results indicate that GRN-2 in the oxidized form induced LLPS of PrLD, while the reduced form induced gelation/aggregation.

Then LLPS/aggregation phase boundaries were determined for GRN-2 and rGRN-2 with PrLD using turbidimetric assays (Fig. 3 e–g). In all these experiments, LLPS and aggregation were differentiated based on microscopic examination of the samples and phase boundaries established by considering an OD_{600} value of 0.140 a.u. as a cut-off for phase transitions (see section "materials and methods"). To see if the negative charges drive GRN-PrLD LLPS, phase separation was observed at two different pHs: at pH 6.0 where the acidic residues have a net negative charge, and at pH 4.5 where the negative charge of acidic residues attenuated from net charge per residue (NCPR) of 0.07 to 0.01 (Table S1). Although the histidine-tagged PrLD is more positively charged at pH 4.5 (þ0.06 NCPR) than at pH 6.0 (þ0.02 NCPR), it does not seem to affect phase separation with GRN-2, as the PrLD without His-tag showed no LLPS (Fig. S11 e). At pH 4.5, no phase separation was observed for GRN-2 or rGRN-2 with PrLD (Fig. 3 e, pH 4.5, and Fig. S11 e), but, at pH 6.0, the proteins underwent phase transitions uniformly at a concentration of 10 mM GRN-2 or rGRN-2 in all PrLD concentrations tested (Fig. 3 e, pH 6.0). However, in stark contrast, under fully reducing conditions, co-incubations of rGRN-2 with PrLD showed gelation/aggregation. The phase diagrams of GRN-3 and GRN-5 with PrLD reveal both similarity and disparity in their phase transitions, as previously observed (50) (Fig. 3 f–g). In an acidic environment, neither GRN-3 nor GRN-5 in both redox conditions undergoes phase

transition with PrLD (Fig. 3 f), similar to GRN-2. At pH 6.0, both oxidized and reduced forms of GRN-3 show gelation/aggregation exclusively, albeit with a delay (solid precipitates observed after 24 h), while incubation with GRN-5 showed LLPS exclusively (Fig. 3 g) (50). Together, these results suggest that the negatively charged residues on GRNs (evident from GRN-5, and data from assays at pH 4.5) are significant contributors of the coacervation with PrLD, while an increasing number of positive charges on the protein modulates the dynamics toward gelation/aggregation (as observed from GRN-2 and GRN-3). Next, we questioned whether GRN-PrLD coacervation was driven by electrostatic interactions, in which case LLPS will be sensitive to salt concentrations. To investigate this, turbidities of different stoichiometric incubations of PrLD and GRN-2 with increasing NaCl concentrations were measured. The data showed progressive decrease in turbidity values with increasing salt concentrations likely due to disruption of electrostatic interactions by NaCl and thus confirming electrostatically driven phase separation between GRN-2 and PrLD (Fig. 3 h). The effect was most prominent in samples containing higher concentrations of the two proteins (Fig. 3 h). Similar titrations were performed on samples of PrLD (varying concentrations) and GRN-2 alone (Fig. 3 i). We observed that samples of PrLD alone (5 mM, 10 mM, 20 mM) initially displayed a lack of turbidity, which increased as titration with NaCl proceeded (Fig. 3 i). In contrast, no rise in turbidity was observed for samples containing 40 mM GRN-2 alone (Fig. 3 i). We also investigated the potential role of hydrophobic residues in mediating LLPS by treating the condensates of GRN-2-PrLD with 1,6-hexanediol (HD), an agent that is known to disrupt weak hydrophobic interactions and dissolve droplets (87,88). Post-treatment analysis showed persistence of the condensates even after treatment with 10% HD (top panels, Fig. 3 j), as shown by turbidity values, albeit with a 45% reduction in their levels compared with pre-HD-treated sample. This suggests that hydrophobic interactions contribute to LLPS to some degree. Similar treatments of HD to PrLD-RNA coacervates showed a 15% decrease in turbidity, reaffirming that LLPS involving the two was driven mainly by electrostatic interactions (middle panels, Fig. 3 j). In contrast, homotypic coacervation of PrLD induced by salt (300 mM) showed dissolution as much as 90% of droplets upon HD treatment (bottom panels, Fig. 3 j) suggesting that the salt-induced phase separation is predominantly driven by hydrophobic interactions, as proposed earlier (89). Together, the data suggest that GRN-2-PrLD coacervation is an electrostatically driven process. Finally, the temperature dependence of PrLD-GRN-2 phase transitions was examined to establish the upper critical solution temperature (UCST) (54,90). As expected, PrLD underwent self-coacervation in no-salt conditions at 4C that was attenuated at 25C, suggesting a UCST between these temperatures (Fig. 3 k). Co-incubation with GRN-2 increased UCST to >49C, while the sample with rGRN-2 showed gelation/aggregation in all the temperature range recorded (Fig. 3 k).

Negatively charged residues in GRNs drive LLPS, while the positively charged ones enhance gelation or aggregation

The pH dependence on phase transitions (Fig. 3 e and f) and HD treatment (Fig. 3 j) provided important clues regarding the involvement of electrostatic interactions, especially the negatively charged residues. To further investigate these in detail, the phase behavior of the three GRNs, GRN-2, -3, and -5, along with specific mutants of GRN-2, were investigated. As mentioned above, all three GRNs are isoelectronic with respect to the negative charges (7, 6, and 6, respectively) but contain a varying number of positively charged residues (þ2, þ4 and 0, respectively) (Fig. 2). As previously shown (50), microscopic investigations of GRN-3 incubated with PrLD in both redox states showed aggregation (saffron box), while GRN-5 showed LLPS (green box) under both redox conditions (Fig. 4 a and b). FRAP confirmed the observations with a rapid recovery for GRN-5 (liquid) and attenuated recovery for GRN-3 (solid) (Fig. 4 a and b). On the other hand, GRN-2 showed LLPS in the oxidized state and aggregation in the reduced state (Fig. 4 c). This suggests that the number of positive charges in GRN-2 is enough to mitigate LLPS in the reduced state but not enough to attenuate LLPS and promote aggregation in the oxidized state. We conjectured that, while negative charges on the GRNs promote LLPS, the positively charged residues tend to shift the equilibrium toward aggregation and solid aggregates. To further substantiate the role of positive charges, a construct was generated in which the two positive charges on GRN-2 were mutated to glutamate (negatively charged) residues to generate a GRN-2 (þ/) mutant that was devoid of any positive charges (net 9 charge), which rendered the mutant similar to GRN-5 electrostatically. If our hypothesis was correct, abrogation of all positively charged residues would promote LLPS in both oxidized and reduced states, identical to GRN-5. Co-incubation of GRN-2 (þ/) and PrLD did show formation of liquid droplets in both fully oxidized and reduced conditions (Fig. 4 d), further cementing our hypothesis that negative charges drive LLPS. To further illustrate this, GRN-7, which has the same number of acidic (6) residues as the other GRNs but has high number of basic residues (þ8), with an overall positive charge (þ2), was co-incubated with PrLD (Fig. S5 a). Based on the inferences drawn thus far, enrichment in positively charged residues should drive aggregation/gelation of PrLD, which was confirmed by the presence of solid aggregates on the co-incubated sample monitored for 36 h (Fig. S5 c). Unfortunately, deeper investigations on GRN-7 were precluded by the difficulties in obtaining pure protein, which was susceptible to substantial

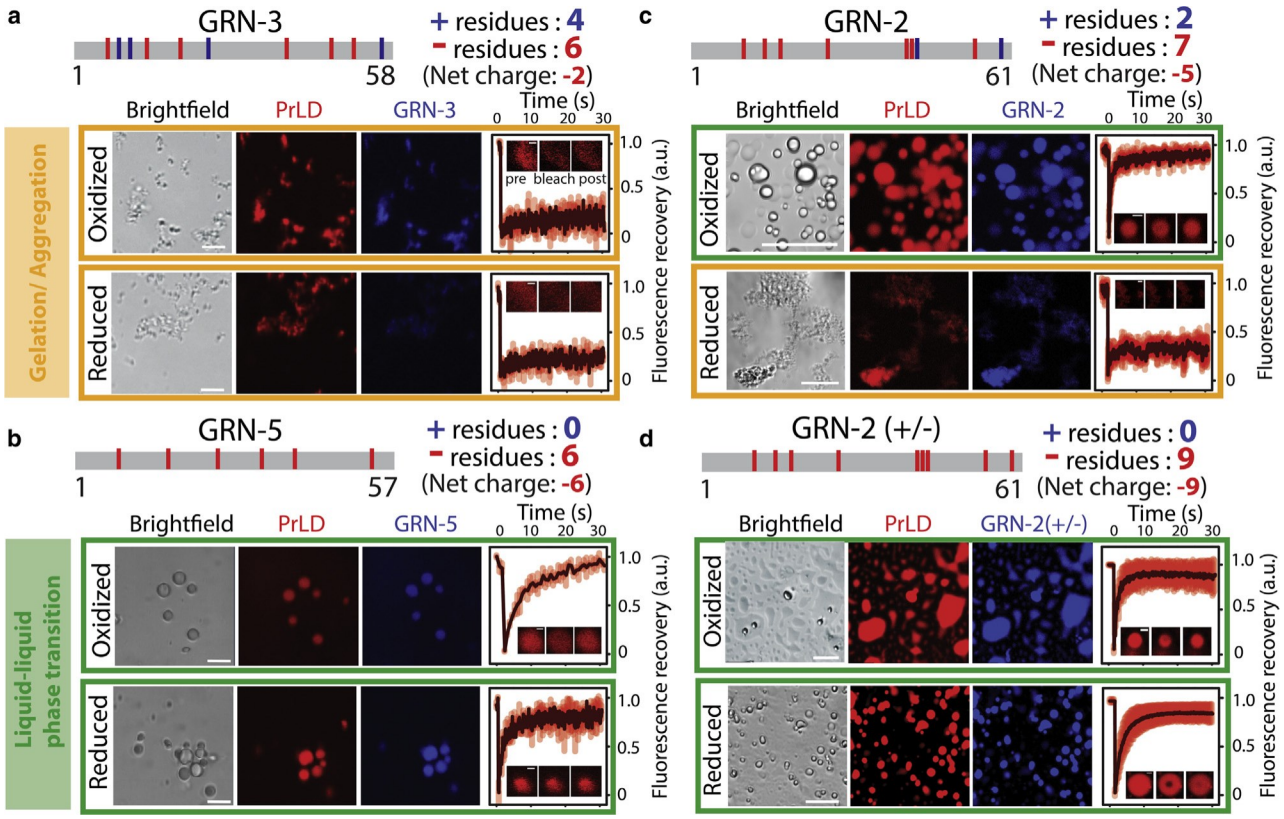

FIGURE 4 Phase transitions of GRNs and specific mutants. (a–d) Sequence of GRN-3, GRN-5, GRN-2, and GRN-2(þ/) annotated with negative and positive charges present and the net charges on the protein at neutral pH (top of each panel). Individual samples are generated by mixing the respective GRN at 40 mM with 20 mM PrLD, along with 1% (molar) fluorophore-labeled proteins (GRNs are labeled with HiLyte-405 and PrLD with HiLyte 647) buffered in 20 mM MES, pH 6.0. Samples were visualized by fluorescence microscope and their internal dynamics were analyzed by performing FRAP analysis on labeled PrLD (HiLyte-647). Individual micrographs are highlighted with a green border for LLPS and a saffron border for gelation/aggregation. The fluo-rescence recovery curves were normalized based on pre-bleaching fluorescence intensities. The insets show pre-bleach, post-bleach, and recovery from left to right. Scale bar represents 10 mm. The images are representatives from at least three independent data points (n ¼ 3). To see this figure in color, go on-line.

proteolytic degradation (data not shown). Last, we evaluated the droplets formed by these proteins with PrLD (Fig. S8). The droplet area (mm^2) of GRN-2 with PrLD shows a normal distribution centered at 25 mm^2 (Fig. S8, gray), which is similar to that observed for GRN-2(þ/) with PrLD (Fig. S8, red). On the other hand, droplets formed in the reaction with rGRN-2(þ/) and PrLD show noticeable reduction in surface areas with a normal distribution centered at 10 mm^2, suggesting diminished ability of the reduced form to undergo LLPS. Furthermore, to ascertain the contribution of hydrophobic aromatic residues in LLPS, F, Y, and W residues of GRN-2 were mutated to A to generate GRN-2DAro mutant. Unfortunately, a significant degree of thiol oxidation to sulfinic acid was observed in this mutant when expressed (Fig. S9 a). Co-incubation of GRN-2DAro with PrLD showed amorphous deposits with no recovery in FRAP, suggesting the solid nature of the deposits (Fig. S9 b). However, precise contributions of aromatic residues were undeterminable due to the formation of highly hydrophilic sulfinic acid due to oxidation, which occurs possibly because of solvent-exposed thiols in the absence of a hydrophobic core in GRN-2DAro.

The redox state of cysteines in GRNs further tunes phase behavior of PrLD coacervates

It is now clear that the coacervation of GRN and PrLD is driven predominantly by electrostatic interactions, while negative charges on GRNs drive LLPS the increase in the number of positive charges shift the equilibrium toward aggregation. However, the role that the oxidation state of thiols plays in this process remained unclear. Therefore, to understand their effect on PrLD phase transitions, microscopic analysis was performed on the co-incubations of GRN-2 and PrLD as a function of a reducing agent (Fig. 5). To mimic local redox fluxes within the cellular cytoplasm (91), the reactions containing 40 mM GRN-2 and 20 mM PrLD with increasing concentrations (50–600 mM) of the reducing agent TCEP were probed by fluorescence microscopy (Fig. 5 a). The TCEP concentrations used generate

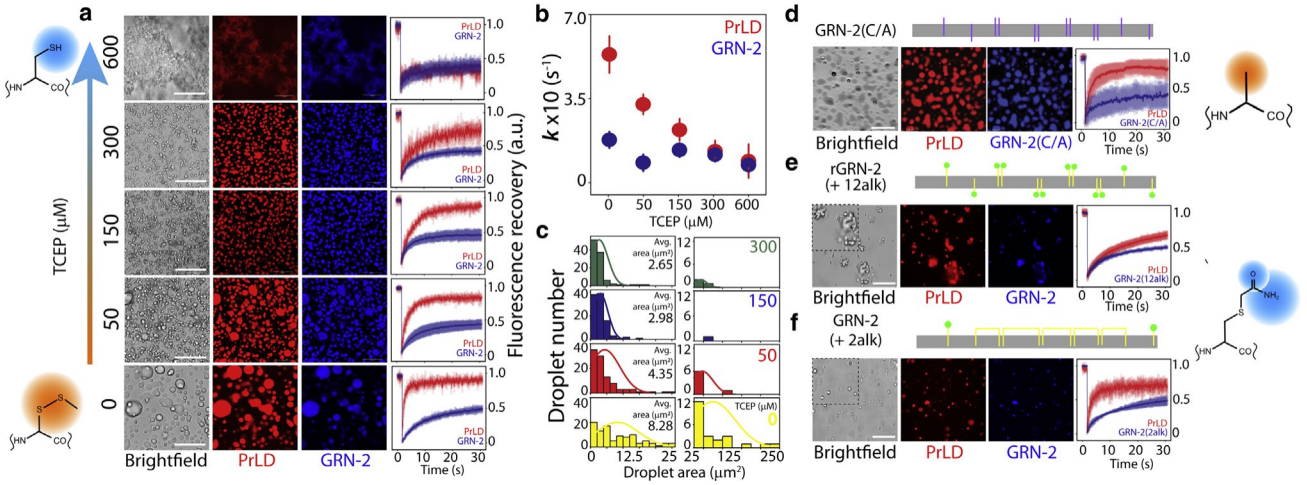

FIGURE 5 Redox state of GRN-2 fine-tunes the phase transitions with PrLD. (a) Reactions containing 20 mM PrLD with 40 mM GRN-2 were initiated separately with increasing TCEP concentrations (50–600 mM) buffered in 20 mM MES, pH 6.0. The hydrophobic and hydrophilic environments around oxidized and reduced cystines, respectively, are schematically presented. (b) Samples were visualized by fluorescence microscopy and probed with FRAP recovery (n ¼ 3). Individual recovery rates of PrLD (red) and GRN-2 (blue) in the reactions of (a) obtained using the initial rate method (n ¼ 3; detailed in section "materials and methods"). (c) Distributions of droplet area (mm^2) observed within the micrographs of reactions in (a). The droplet area distributions were extracted using ImageJ where a total of 100 droplets was considered for each sample from at least nine, 20 20-mm independent fields from two independent experiments, and normal distribution are plotted (detailed in section "materials and methods"). (d) Schematic depicting the GRN-2(C/A) mutant (cysteines replaced with alanines; purple vertical bars). The micrographs represent reactions of 20 mM PrLD with 40 mM GRN-2(C/A) buffered in 20 mM MES, pH 6.0 along with the FRAP analysis on both labeled PrLD (red; HiLyte-647) and GRN (blue; HiLyte-405). (e and f) Mi-crographs of mixtures containing 40 mM alkylated GRN-2 (e, 2-free thiols alkylated; f, 12-free thiols alkylated) generated using iodoacetamide, with 20 mM PrLD along with the FRAP analysis. For visualization using fluorescence microscopy, all samples contained 1% fluorophore-labeled proteins (GRN-2, GRN-2(C/A), and alkylated forms were labeled with HiLyte-405, while PrLD was labeled with HiLyte-647. All reactions were initiated and imaged at room tem-perature. Scale bar represents 20 mm. To see this figure in color, go online.

partially reduced (50–300 mM) to completely reduced (600 mM) thiols in GRN-2. In the absence of the reducing agent, GRN-2, as expected, underwent LLPS with PrLD forming liquid droplets that undergo fusion and coalescence as observed previously (0 mM TCEP; Fig. 5 a). To ascertain the droplets' fluid-like properties, their internal dynamics were analyzed by FRAP, which showed a rapid recovery for PrLD, reiterating an archetypal fluidic characteristic of the droplets (red curve, 0 mM TCEP; Fig. 5 a). For reasons unclear at this time, attenuated mobility for the colocalized GRN-2 within the liquid droplets was observed, as seen in its recovery curve (blue curve, 0 mM TCEP; Fig. 5 a). The observed LLPS by oxidized GRN-2 could also arise from the network of intra-molecular disulfide bonds that limit the solvent accessibility of some of the stickers in the sequence. This, in part, is supported by the attenuated FRAP recovery rates for GRN as opposed to PrLD (Fig. 5 a and b) and the solvent exposure of the single tryptophan residue in the middle of the sequence in oxidized and reduced states (Fig. S10).

In the presence of 50 mM TCEP (partially reducing conditions), the magnitude of droplet formation was dampened and structures with an altered morphology were visible alongside spherical droplets (50 mM TCEP; Fig. 5 a). Increasing concentrations of TCEP (150–600 mM) showed numerous smaller droplets and a progressive decrease in fluorescence recovery rates for PrLD (Fig. 5 a and b). The rate constant (k) deduced by an initial-rate method from the FRAP data showed a first-order kinetics for PrLD recovery as a function of reducing agent concentrations, while GRN-2 showed a diminished rate of recovery in fully oxidized and partially reduced (50 mM TCEP) conditions (Fig. 5 b). In fully reducing conditions, the mixture of rGRN-2 and PrLD underwent aggregation, as observed previously (Figs. 3 and 4), generating solid, fibril-like aggregates and was devoid of any droplets, as confirmed via microscopy and FRAP data (600 mM TCEP; Fig. 5 a). The use of other reducing agents, such as dithiothreitol (DTT) and glutathione (GSH), also showed similar results (Fig. S6). Furthermore, analyses of droplet size as a function of the reducing agent provided some interesting insights (Fig. 5 c). The droplet size distributions, in terms of the surface area, were consolidated into two categories of small (area <25 mm^2) and large droplets (25 < area <250 mm^2). The coacervates in fully oxidized conditions showed a wide distribution of droplet sizes. The surface areas of small droplets were centered at 10 mm^2, with an average droplet size of 8.2 mm^2 (yellow, Fig. 5 c). In addi-tion, a notable number of droplets larger than 25 mm^2 were also observed in the sample with an average surface area of 60–70 mm^2 (yellow, Fig. 5 c). Increasing TCEP concentra-tions (50–600 mM) revealed a discernible shift toward smaller droplet distributions with average surface areas of 4.35, 2.89,

and 2.65 mm^2 for 50, 150, and 300 mM TCEP concentrations, respectively (Fig. 5 c). We attribute this behavior to the reduction in surface tension introduced by way of thiol solvation or hydrogen-bonding interactions.

These results bring out two important points: first, the modulation of phase transitions by potential redox fluctuations does not seem to be abrupt but requires a complete reduction of cysteines to promote gelation or aggregation. Second, cysteine thiols seem to play a role in shifting the equilibrium from the liquid to the gelated/aggregated phase, possibly due to a hydrophilic environment generated and by engaging in hydrogen-bonding interactions with bulk water (solvation) and/or with PrLD (Fig. 5 a). If this is the case, we argued that abrogation of cysteines (and, therefore, thiols) will cause GRN-2 to behave as in fully oxidizing conditions. To test this, all 12 cysteines in GRN-2 were mutated to alanines to generate a GRN-2(C/A) mutant. Indeed, co-incubation of PrLD with GRN-2(C/A) showed the formation of liquid droplets, with rapid fluorescence recovery confirming a fluid-like character (Fig. 5 d). The similarity in the behavior of GRN-2(C/A) and GRN-2 is also apparent from the droplet size observed (Fig. S8). The droplet areas of the mutant form (Fig. S8, green) have a similar distribution to that of the wild type (Fig. S8, gray), with an average value of 25 mm^2. On the contrary, when all the free thiols in the fully reduced form of rGRN-2 were alkylated and cap-ped with acetamide (GRN-12alk), a moiety, which is ex-pected to be both solvated by bulk water and engage in hydrogen-bonding interactions with PrLD perhaps to a greater extent than thiols, the coacervates formed solid-like structures with attenuated internal mobility as revealed by FRAP (Fig. 5 e). Similarly, acetamide alkylation of two free thiols present in the fully oxidized samples (Fig. S4), which mimics partially reducing conditions, also showed no change from those incubated in the presence of 50 mM TECP (Fig. 5 f). The effect of solvent interactions with thiols in the reduced state was further supported by our serendipitous discovery with GRN-2DAro mutant. Despite stringent experimental precautions to prevent oxidation of thiols during expression and purification, GRN-2DAro mutant showed that up to five cystine thiols were oxidized to sulfinic acids (Fig. S9 a). Since sulfinic acids are strongly hydrophilic, they are likely to be engaged in hydrogen-bonding interactions with the solvent water. In such a case, based on the data obtained so far, one would expect aggregation of PrLD in the presence of GRN-2DAro, which is exactly what was observed (Fig. S9 b). Together, the data bring to light the role of cysteine in phase transitions of PrLD and GRNs, which is one of modulatory nature, fine-tuning the transitions only in GRN-2, which happens to fall in category of partially counterbalanced positive and negative charges. As observed before (50), GRN-3 and -5 showed no effect on respective phase transitions due to the extremity of the electrostatics in their respective cases.

GRN-2 delays but induces ThT-positive aggregates of TDP-43 PrLD in oxidized or reduced states

We have previously shown that the concentration-dependent LLPS of PrLD by GRN-5 or aggregation by GRN-3 are accompanied by a delayed emergence of ThT fluorescence (50), which is a reporter of amyloid-like aggregates (92). To see whether GRN-2 in both redox forms induces ThT-positive PrLD aggregates, the co-incubations of increasing concentrations of GRN-2 or rGRN-2 and PrLD were monitored for 24 h in the presence of ThT (Fig. 6 a). All reactions showed slightly elevated ThT levels at the beginning (0 h; Fig. 6 a) but failed to show sigmoidal increase of ThT fluorescence as observed for the control PrLD (Fig. 6 a). This observation was similar to that observed previously with GRN-3 and GRN-5 (50). AFM images obtained after 60 h of incubation for 1:2 molar ratio of PrLD:GRN-2 showed fibrillar structures even though they were attenuated in ThT intensities (Fig. 6 b). However, stark contrast was visible between the morphologies of the PrLD fibrils and these incubated with GRN, suggesting the possibility of different polymorphic structures. Microscopic investigations of the reactions with GRN-2 showed the formation of liquid droplets in all stoichiometric equivalents immediately after incubation (0h; Fig. 6 c). After 24 h, the droplets continue to be present, although a few of them showed morphological changes suggesting possible gelation (24h; Fig. 6 c). To probe this possibility, we performed FRAP on the structures after a 24-h period. Compared with the fluorescence recovery shown by the liquid droplets of 40 mM GRN-2 with 20 mM PrLD (Fig. 6 c, FRAP, 0 h, red), the distorted droplets in all stoichiometric reactions show attenuation in their recov-ery kinetics (Fig. 6 c, FRAP, 24 h, brown) confirming the progressive gelation of the liquid droplets. In addition, this attenuation positively correlates with GRN-2 concentrations (Fig. 6 c). On the other hand, under fully reducing conditions, incubations of rGRN-2 with PrLD showed an instantaneous formation of insoluble aggregates that persisted after 24 h (Fig. 6 d). However, >60 h of incubations with oxidized and reduced GRN-2 in lower stoichiometric equivalence (up to 1:1 molar ratio) showed increases in ThT intensities toward amyloid-like aggregates (Fig. S7). In contrast, higher molar concentrations of GRN-2 (1:2 molar ratio) led to attenuation of ThT even after 60 h (Fig. S7). Similar attenuation of ThT was also observed in the presence of GRN-7 (Fig. S5 b). As noted above, attenuation of ThT alone cannot be considered as inhibition of amyloid formation as the AFM images clearly showed fibrillar aggregates (Fig. 6 b).

RNA competes and displaces GRN-2 from PrLD coacervates

Under cellular stress conditions, PrLD transfected in SH-SY5Y cells is either found in SGs along with TIA1 or

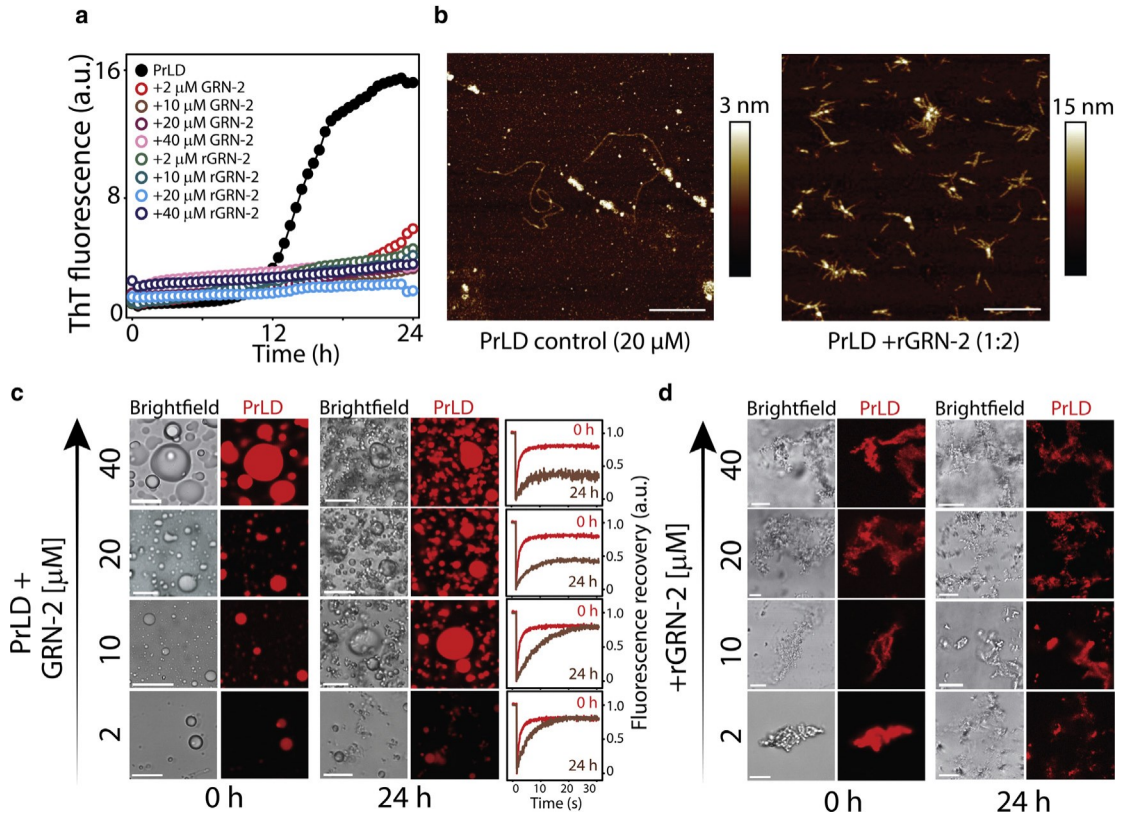

FIGURE 6 Amyloid formation of PrLD in presence of GRN-2. (a) The amyloid formation of 20 mM TDP-43 PrLD alone (C) or in presence of varying concentrations (2–40 mM) of GRN-2 or rGRN-2, buffered in 20 mM MES, pH 6.0, monitored using 15 mM ThT for a period of 24 h at 37C under quiescent conditions. (b and c) Micrographs of reactions in (a) visualized using brightfield and fluorescence microscope with 1% fluorophore-labeled PrLD (HiLyte-647) imaged at 0 h and after an incubation of 24 h. (b) AFM images of the 1:2 molar ratio of PrLD:rGRN-2 along with PrLD control. The scale bar represents 200 nm. (c) The droplets observed initially upon mixing GRN-2 with 20 mM PrLD were subjected to FRAP analysis immediately (0 h, red curve) and after 24 h (brown curve). FRAP analysis was performed on labeled PrLD (HiLyte-647). (d) Microscopic visualization of PrLD in the presence of varying concentrations of rGRN-2 (2–40 mM) shows the formation of solid deposits at 0 h and 24 h. Scale bar represents 10 mm. To see this figure in color, go on-line.

colocalized with GRNs in the cytoplasm, but colocalization of all three was not observed (Fig. S1). We conjectured that it is due to potential competition between GRNs and RNA, in which the latter displaces the former in SGs. To test this, ternary interactions between RNA, GRN-2, and PrLD were investigated in vitro (Fig. 7). PrLD (20 mM) was co-incubated with three GRN-2 concentrations of 10, 20, and 40 mM, and each co-incubated sample was investigated with the addition of increasing RNA (poly-A) concentrations (0–150 mg/mL). The positive control, PrLD, and RNA showed prototypical turbidity increase with increasing RNA concentrations that saturated about 50 mg/mL and showed a slight drop in turbidity at 150 mg/mL (; Fig. 7 a). Increasing RNA concentrations in PrLD-GRN-2 co-incubations also showed similar trends but with higher initial turbidity values (, , and ; Fig. 7 a). Irrespective of the concentration of GRN-2 in the mixture, the eventual turbidity values of all samples converge to that shown by PrLD with 150 mg/mL RNA. This hints at the similar compositional makeup of the final condensates, which is insensitive to GRN-2 concentration in the presence of high RNA concentrations (Fig. 7 a). To probe the internal dynamics of these interactions, we used fluorescence microscopy with fluorophore-labeled proteins and repeated the experimental setup. Co-incubations of varying concentrations of GRN-2 with PrLD, in the absence of RNA, showed droplet formation as expected (0 RNA; Fig. 7 b–e). The addition of increasing amount of RNA to 10 mM GRN-2 incubations showed a steady displacement of GRN-2 (blue) from within the droplet from 50 to 75 mg/mL, while PrLD (red) remained largely unaffected (Fig. 7 c). Between 100 and 150 mg/mL of RNA, GRN-2 has been completely displaced from the droplet (Fig. 7 c). Interestingly, the displacement and substitution of GRN-2 did not occur concertedly but involved the formation of coexisting multiphasic condensates with coacervates of PrLD-RNA engulfing those of PrLD-GRN-2, as deduced by the fluorescence intensity plots (Fig. 7 c).

A similar behavior was also observed with samples containing increased GRN-2 concentrations (20 and 40 mM) (Fig. 7 d and e). Such coexisting heterotypic

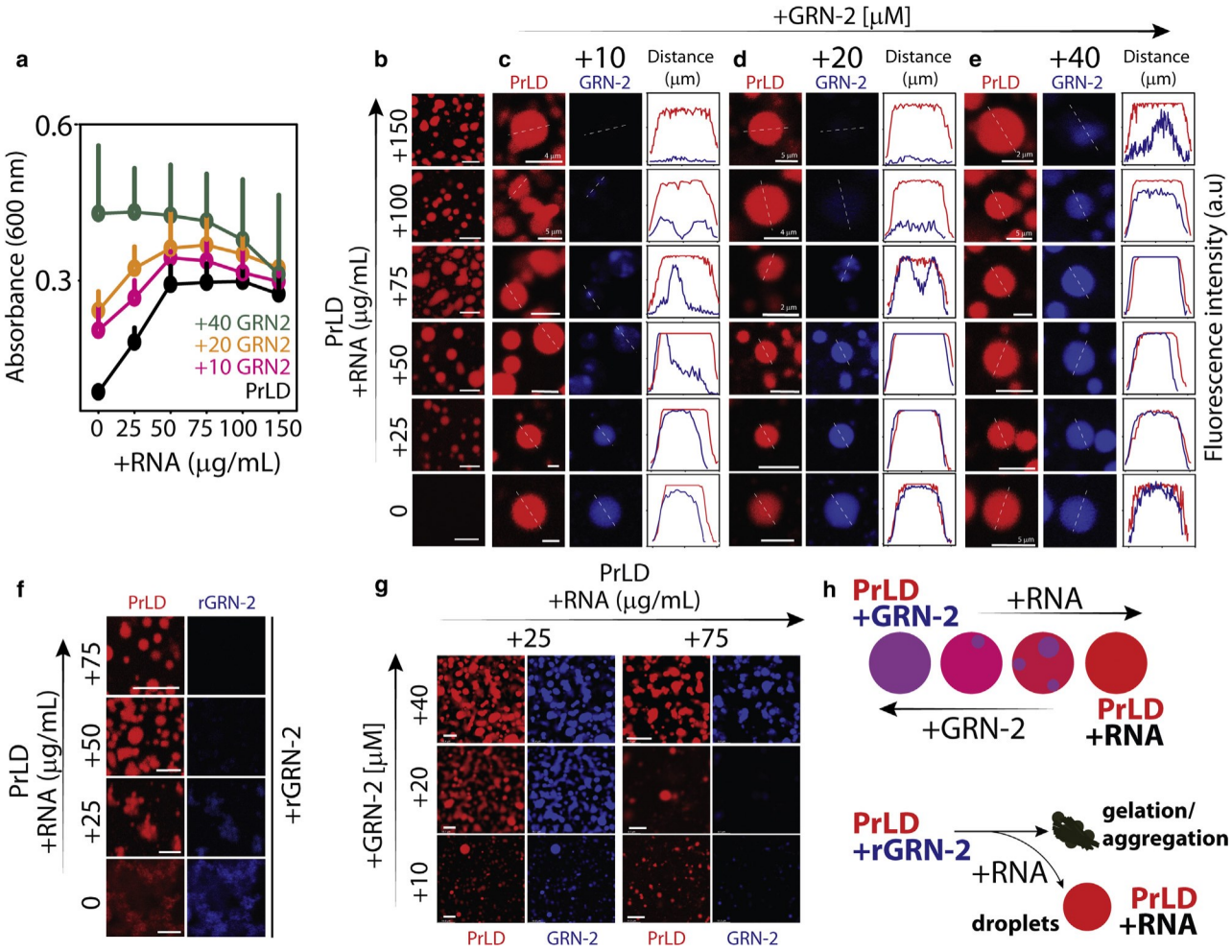

FIGURE 7 Ternary interactions between GRN-2, PrLD, and RNA. (a) Turbidity plots obtained by titrating 20 mM PrLD with increasing RNA concentration (25–150 mg/mL) in the presence (pink, 10 mM; orange; 20 mM or gray, 40 mM GRN-2) or the absence of GRN-2 (C) (n ¼ 3). (b–e) Confocal micrographs depicting selective droplets observed in reactions from (a). Displacement of GRN-2 upon titration with RNA was observed by the fluorescence intensity profiles of the respective fluorophore-labeled proteins (GRN-2 with HiLyte-405 and PrLD with HiLyte-647) and was extracted across the width of the droplets using ImageJ (detailed in section "materials and methods"). (f) Microscopic visualization of complex coacervates of 20 mM PrLD with varying RNA concentrations (25–75 mg/mL) generated initially were titrated with 40 mM rGRN-2. (g) Condensates of 20 mM PrLD with varying RNA concentration (25 or 75 mg/mL) were titrated with increasing GRN-2 concentration (10–40 mM) and were visualized microscopically. (h) Schematic depicting the outcome of ternary interactions among GRN-2, RNA, and PrLD. All reactions were initiated and imaged at room temperature. Unless specified, scale bar represents 10 mm. To see this figure in color, go online.

condensates have also been observed in ternary complexes involved in prion-like polypeptide, RNA, and arginine-rich polypeptides (93). Similar to Kaur and colleagues, we observe a ternary system in which RNA-PrLD interactions outcompete and dominate PrLD-GRN-2 interactions by displacing GRN-2. This also suggests that GRN-2 and RNA are mutually exclusive binding partners for PrLD demixing and LLPS, which in turn explains why GRN-2 is not observed in SGs. Furthermore, we also examined the effect of rGRN-2 on the condensates of PrLD-RNA (Fig. 7 f). Here, condensates of 20 mM PrLD with varying RNA concentrations (25–75 mg/mL) were generated, and 40 mM rGRN-2 was added followed by visualization using fluorescence microscopy. We observed that, at a low RNA concentration (25 mg/mL), rGRN-2 is able to interact with unengaged PrLD within the mixture and drive its aggregation (Fig. 7 f, þ25 RNA) similar to that observed in the absence of any RNA (Fig. 7 f, 0 RNA). In the condensates of PrLD-RNA generated with higher RNA concentrations (50–75 mg/mL), the external addition of rGRN-2 leads to minimal or no aggregation with the sustenance of RNA-PrLD condensates, as seen in the micrographs (Fig. 7 f, þ50 and þ75 RNA). We also performed an inverse experiment where GRN-2 was titrated on PrLD-RNA droplets (Fig. 7 g) and observed that high concentrations of GRN-2 coacervates with PrLD presumably displacing RNA. These results provide potential clues to the absence of GRNs in SGs, which is likely the result of high amounts of RNA (and possibly other proteins) in SGs displacing GRNs (Fig. 7 h).

DISCUSSION

The precise role of GRNs in the pathophysiology of neurodegenerative disorders has remained an open question. Under what conditions and cellular cues they are generated from their percussor PGRN, and what role do they play in cellular functions and dysfunction have been points of debate (44,45,94–97). What we do know is that PGRN secreted from microglia and astrocytes is transported into neuronal lysosomes by a sortilin-mediated pathway (97,98) and its subsequent proteolytic processing generates GRNs within the lysosomes (43,45), but functions of GRNs within lysosomes remain uncertain. PGRN also undergoes proteolytic cleavage extracellularly during chronic inflammation (42) such as in TBI or neurogenerative diseases. The fate of such extracellular GRNs on neuronal functions also remains completely unknown. Here we investigated the possible cellular localization and interaction of extracellular GRNs (GRN-2, -3, and -5) with TDP-43 by treating GRNs onto SHSY5Y neuroblastoma cells that transiently express TDP-43 PrLD. These studies, along with in vitro biophysical investigations on the interactions between the two proteins, have brought out some unexpected properties of GRNs and PrLD that reveal the former's potential role in FTLD and related TDP-43 proteinopathies.

To understand the fate of extracellular GRNs on neurons, we labeled GRNs with organic fluorophores (HiLyte) to visualize their uptake, but not with protein-based tags that may predispose them for specific cellular localization. The data indicate that the GRNs are taken up by SH-SY5Y cells to be localized not only within the lysosomes (well known) but also in the cytoplasm. More importantly, GRNs colocalize with TDP-43 PrLD in the cytoplasm both under stress and non-stress conditions, indicating their potential involvement in FTLD and ALS pathologies (Fig. 1). Furthermore, under stress conditions, based on the lack of FRAP recovery and absence of colocalization with the SG marker TIA1 (Fig. S1), we could infer that GRNs are not likely to partition within the SGs. In addition, we infer that the cytosolic colocalizations observed are complex cytoplasmic coacervates of PrLD and GRNs. Interestingly, unlike with PrLD, GRNs failed to co-localize with full-length TDP-43 under either non-stress conditions or stress conditions (within SGs) (Fig. S2), illustrating that GRNs may specifically interact with the pathogenic proteolytic PrLD-containing fragments of TDP-43 (99), further implicating their role in pathology.

The dynamics of interactions between GRN-2 and PrLD investigated here have furthered our understanding of the possible mechanisms by which GRNs could modulate intracellular inclusions of TDP-43. Coacervation of TDP-43 with RNA has been known to be electrostatically driven (78,81). In the present study, we have used PrLD containing an N-terminal hexa-histidine tag (Fig. 2 a). We observed that cleavage of the tag prohibitively decreases the yields of the protein for biophysical investigations as also reported by others (100). Furthermore, the hexa-histidine tag was computed to carry only a slight overall positive charge at pH 6.0 (101); the presence of D, E, and K residues alongside the histidine tag in the linker further nullifies positive charges and possesses a net negative charge for this segment, and, therefore, we believe the tag does not contribute to phase separation. This was further confirmed by our results with histidine-tag-removed PrLD, which did not show differences in its phase separation behavior with GRNs (Fig. S11), as observed previously by other groups also (50), dismissing the possibility of tag contributing to phase separation. It has to be borne in mind that negatively charged residues in PrLD are likely to play a role in the phase transitions with GRNs. However, our focus in this work is to uncover how charge patterns on the GRNs influence phase modulations with PrLD. To this effect, wild-type PrLD was held constant as an unchanged parameter so as to analyze only the sequence contributors on GRNs; i.e., no mutations or post-translational modifications were made on PrLD to dissect its sequence contributions, although this is of great interest for our future and ongoing investigations.

Earlier, we showed that coacervation with GRNs is likely driven by the net charges on the protein (50). The charge distributions on GRN-2, -3, and -5 show that they have similar number of negative charges (7) but vary in the number of positive charges; GRN-2 with þ2 is in the middle between GRN-3 and -5, which have þ4 and 0 positively charged residues, respectively) (Fig. 2). While the net charge on GRN-2, -3- and -5 is negative (4.21, 2.03, and 6.00, respectively), GRN-7 has net positive charge (þ2.78) (Table S1). This trend is also re-flected in the NCPR values (Table S1). Hydropathy indices of all these GRNs are similar (4.50) except for GRN-7 (3.90) (Table S1). This facilitated the investiga-tions on GRN-2's interactions with PrLD to draw bio-physically meaningful inferences as GRN-3 and -5 have been shown to display a spectrum of phase transitions upon interacting with PrLD (50). The results presented here establish that the negative charges are the main driving forces of LLPS between GRNs and PrLD, while the increase in the number of positive charges shifts the equilibrium toward aggregation (Fig. 8 a). To a lesser degree, hydrophobic interactions may also contribute but certainly do not seem to drive LLPS. Interestingly, by simply modulating the charges on GRNs, one could seemingly control the dynamics of phase transitions and coacervation with PrLD, as summarized in Fig. 8 b–g. When under the control of purely negative charges on GRN, PrLD undergoes LLPS to form droplets that are demixed from the solution (Fig. 8 b and c). This can be explained based on polyphasic linkage and ligand binding effect on phase transitions as recently postulated by Ruff and coworkers (102). Based on their work, preferential

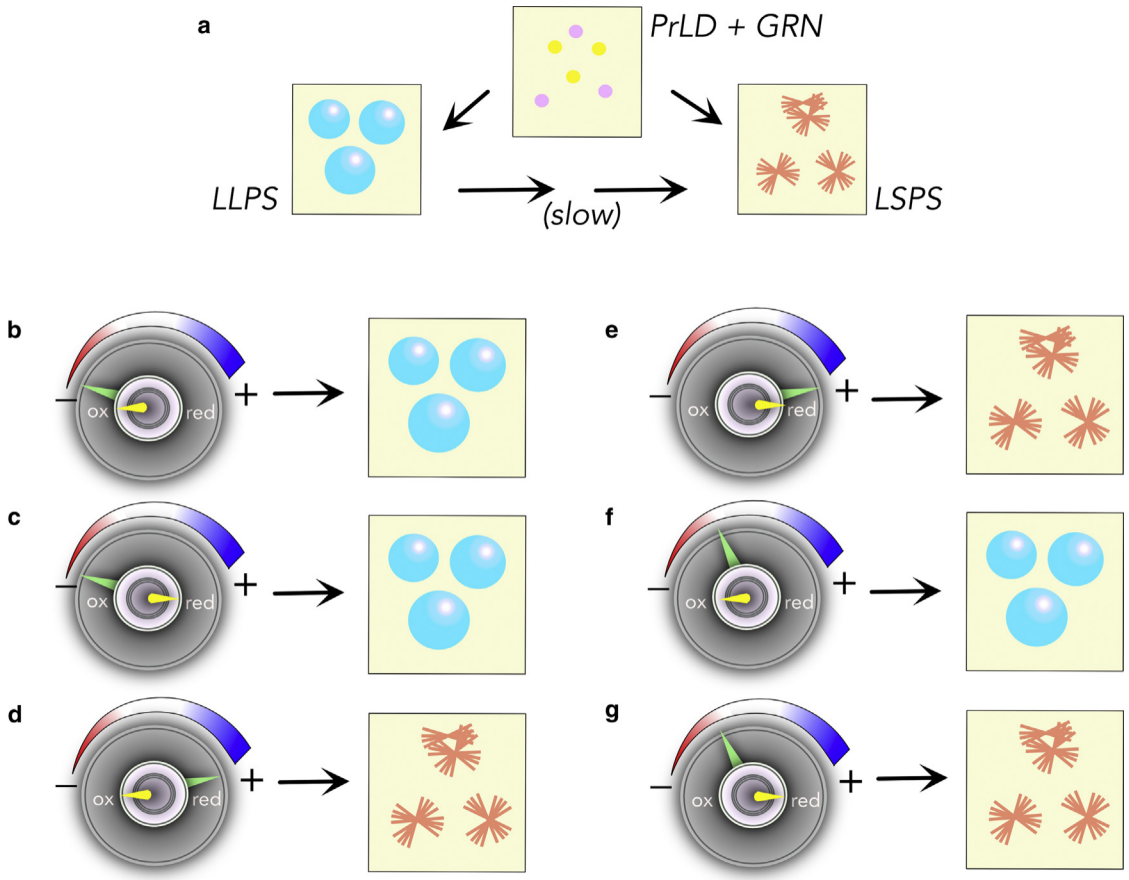

FIGURE 8 Schematic summary of coacervation between GRNs and PrLD. (a) Phase transitions of PrLD induced by GRNs. (b–g) Phase changes are coarsely controlled by electrostatic interactions (large knob), while they are finely controlled by the redox state (smaller knob) for some select conditions discovered in this report. To see this figure in color, go online.

binding of a ligand (GRN) to the scaffold (PrLD) in dilute or dense phase can be expressed as

$$C_{dil;\,L} \;¼\; C_{dil}\;\frac{P_{dil}}{P_{den}}$$

where $C_{dil,L}$ is concentration of the scaffold in the coexisting dilute phase in ligand's presence, and P_{dil} and P_{den} are binding polynomials that define ligand binding to the scaffold in respective phases. If $P_{dil} > P_{den}$, i.e., binding of ligand to the scaffold is greater in the dilute phase, $C_{dil,L} > C_{den}$, LLPS gets suppressed and when $P_{dil} < P_{den}$ LLPS is augmented. Therefore, negative charges potentiate multivalent electrostatic charges with PrLD to preferentially partition into the dense phase, thus promoting LLPS. Increasing the number of positive charges to þ4 shifts the equilibrium toward the formation of solid aggregates possibly by engaging in additional salt-bridge interactions with acidic residues of PrLD, preferably in the dilute phase (Fig. 8 d and e). These interactions, we speculate, also promote aggregation. Unfortunately, we do not have experimental evidence for this extreme case (high positive charges and no negative charges), because such a mutant posed difficulty in recombinant expression in E. coli and thus could not be purified (data not shown). However, the results obtained from GRN-7 (Fig. S5), which has a high number of positive charges (þ8), serves as a good proxy and strengthens the validity of the idea that GRNs have modulatory capabilities, especially when it is known that not all GRN levels are the same in cells (103).

Perhaps the most interesting aspect of phase transitions between PrLD and GRNs is the role of cysteines and redox control. Our data indicate that, when under compensatory positive and negative charge regimes in GRNs, redox conditions dictate the phase transitions (Fig. 8 f and g). Under fully reducing conditions, thiols in cysteines may participate in a network of hydrogen-bonding interactions with Ser and/or Asn residues that are abundant in PrLD. Both these residues are conducive partners of cysteines as hydrogen-bonding donors and acceptors (104) and are abundant in PrLD (together accounting for 25% of the sequence). Empirically, it is evident that these additional valences increase solute-solute interactions that shift the equilibrium out of the liquid-like state toward an aggregated state. The possibility of such a scenario is supported by the behavior of the alkylated forms of GRN-2 (Fig 5), where the polar

acetamide adducts can engage in similar interactions. However, under oxidizing conditions, the disulfide-bonded cysteines that preclude such interactions are abrogated, and therefore maintain weak and transient interactions that promote LLPS and a demixed state. From this, we surmise that the positively charged residues and thiols help fine-tune the phase transitions. It is important to note that not an abrupt change but a continuum of phase changes is observed when traversing from one end of the redox spectrum to the other (Fig 5), which indicates that, even under partially reducing conditions, LLPS can occur, albeit to a lesser degree. Therefore, it seems plausible that GRN-PrLD droplets and aggregates could co-exist in the cytoplasm, which largely presents a reducing environment.

The data presented here unambiguously establish coacervation between PrLD and GRNs, but the absence of GRNs in SGs within PrLD or full-length TDP-43 expressing neuroblastoma cells seems counter-intuitive at the outset. However, the ternary interactions between PrLD, GRN-2, and RNA offer clues for the inability of GRNs to partition into SGs. GRN within the condensates of PrLD simply gets displaced by a stronger electrostatic ligand, RNA, which abrogates the possibility of the three coexisting within the SGs. Given that SGs also contain many other phase-separating proteins, such as TIA1 (66), G3BP1 (105), and hnRNPA1 (106), the likelihood of GRNs partitioning into SGs is probably low. Furthermore, it is also interesting to observe that RNA can outcompete GRN-2 in reducing conditions, where it forms insoluble aggregates with PrLD (Fig 7). This, along with the observed colocalization of GRN and PrLD as puncta in both non-stress and stress conditions, suggests that SGs could partly mitigate the potential toxicity posed by GRN-PrLD inclusions, which eventually transition to amyloids, with an intervening gelated phase.

This report also brings out the first evidence for the cellular uptake of extracellular GRNs and their cytoplasmic colocalization with PrLD. The exquisite control and tuning of coacervation of PrLD by GRNs via electrostatics and redox flux present intriguing possibilities by which GRNs can influence pathology. During acute inflammation, when GRNs are known to be generated in abundance by microglia and astrocytes (42,107–109), these pro-inflammatory molecules are taken up by neurons, where they modulate the dynamics of cytotoxic proteolytic fragments of TDP-43. Even with haploinsufficiency of PGRN, which is a risk factor for FTLD, it can be conjectured that inflammation could lead to augmented production of GRNs that could compensate for the loss in PGRN (42). Perhaps the most interesting aspect when observing the sequence of the seven GRNs is that they seem to have a perfect combination and spectrum of positive and negative charges to eloquently modulate TDP-43 phase transitions. It also seems to be that the extracellular cleavage of PGRN may be asymmetric, leading to a greater abundance of one GRN over another (106), which could play a role in the modulation of TDP-43. Nevertheless, precisely what cellular consequences these inclusions and coacervates possess remains unclear at this time. A few possibilities include induction of mitochondrial, lysosomal, and autophagic dysfunction. Some of these will be unearthed in the coming years with the establishment of complex interactions and phase transitions between GRNs and TDP-43 PrLD, as described in this report.

SUPPORTING MATERIAL

Supporting material can be found online at https://doi.org/10.1016/j.bpj.2022.04.034.

AUTHOR CONTRIBUTIONS

V.R. conceptualized the project. A.A.B. performed protein expression and biophysical experiments. S.D. performed the cell culture experiments. H.G.A. and S.M. performed AFM experiments. V.R., A.A.B., and S.D. participated in intellectual discussions and manuscript writing and editing.

ACKNOWLEDGMENTS

The authors would like to thank the following agencies for financial support: National Institute on Aging (1R56AG062292-01) and the National Science Foundation (NSF CBET 1802793) to V.R. The authors also thank the National Center for Research Resources (5P20RR01647-11) and the National Institute of General Medical Sciences (8 P20 GM103476-11) from the National Institutes of Health for funding through INBRE for the use of their core facilities, and the National Science Foundation (NSF MRI 2019023) for STED confocal microscope facility. The authors would also like to thank Dr. Jonathan Lindner for his gracious help with the confocal microscope use and troubleshooting.

DECLARATION OF INTERESTS

The authors declare that they have no financial or non-financial interests.

REFERENCES

1. Bang, J., S. Spina, and B. L. Miller. 2015. Frontotemporal dementia. Lancet. 386:1672–1682. https://doi.org/10.1016/s0140-6736(15)00461-4.
2. Seelaar, H., J. D. Rohrer, . , J. C. van Swieten. 2011. Clinical, genetic and pathological heterogeneity of frontotemporal dementia: a review. J. Neurol. Neurosurg. Psychiatry. 82:476–486. https://doi.org/10.1136/jnnp.2010.212225.
3. Grossman, M. 2002. Frontotemporal dementia: a review. J. Int. Neuropsychol. Soc. 8:566–583. https://doi.org/10.1017/s1355617702814357.
4. Prasad, A., V. Bharathi, ., B. K. Patel. 2019. Molecular mechanisms of TDP-43 misfolding and pathology in amyotrophic lateral sclerosis. Front. Mol. Neurosci. 12:25. https://doi.org/10.3389/fnmol.2019.00025.
5. Irwin, D. J., N. J. Cairns, . , J. Q. Trojanowski. 2015. Frontotemporal lobar degeneration: defining phenotypic diversity through personalized medicine. Acta Neuropathol. 129:469–491. https://doi.org/10.1007/s00401-014-1380-1.
6. Sun, Y., and A. Chakrabartty. 2017. Phase to phase with TDP-43. Biochemistry. 56:809–823. https://doi.org/10.1021/acs.biochem.6b01088.
7. François-Moutal, L., S. Perez-Miller, . , M. Khanna. 2019. Structural insights into TDP-43 and effects of post-translational modifications.

Front. Mol. Neurosci. 12:301. https://doi.org/10.3389/fnmol.2019.00301.

8. Buratti, E., and F. E. Baralle. 2008. Multiple roles of TDP-43 in gene expression, splicing regulation, and human disease. Front. Biosci. 13:867–878. https://doi.org/10.2741/2727.
9. Buratti, E., T. Dörk, . , F. E. Baralle. 2001. Nuclear factor TDP-43 and SR proteins promote in vitro and in vivo CFTR exon 9 skipping. EMBO J. 20:1774–1784. https://doi.org/10.1093/emboj/20.7.1774.
10. Wang, H. Y., I. F. Wang, . , C. K. Shen. 2004. Structural diversity and functional implications of the eukaryotic TDP gene family. Genomics. 83:130–139. https://doi.org/10.1016/s0888-7543(03)00214-3.
11. Khalfallah, Y., R. Kuta, . , C. Vande Velde. 2018. TDP-43 regulation of stress granule dynamics in neurodegenerative disease-relevant cell types. Scientific Rep. 8:7551. https://doi.org/10.1038/s41598-018-25767-0.
12. Herman, A. B., M. Silva Afonso, . , M. V. Autieri. 2019. Regulation of stress granule formation by inflammation, vascular injury, and atherosclerosis. Arteriosclerosis, Thromb. Vasc. Biol. 39:2014–2027. https://doi.org/10.1161/atvbaha.119.313034.
13. Liu-Yesucevitz, L., A. Bilgutay, . , B. Wolozin. 2010. Tar DNA binding protein-43 (TDP-43) associates with stress granules: analysis of cultured cells and pathological brain tissue. PLOS One. 5:e13250. https://doi.org/10.1371/journal.pone.0013250.
14. Colombrita, C., E. Zennaro, . , A. Ratti. 2009. TDP-43 is recruited to stress granules in conditions of oxidative insult. J. Neurochem. 111:1051–1061. https://doi.org/10.1111/j.1471-4159.2009.06383.x.
15. Van Treeck, B., D. S. W. Protter, . , R. Parker. 2018. RNA self-assembly contributes to stress granule formation and defining the stress granule transcriptome. Proc. Natl. Acad. Sci. U S A. 115:2734–2739. https://doi.org/10.1073/pnas.1800038115.
16. Protter, D. S. W., and R. Parker. 2016. Principles and properties of stress granules. Trends Cell Biology. 26:668–679. https://doi.org/10.1016/j.tcb.2016.05.004.
17. Mackenzie, I. R. A., and R. Rademakers. 2008. The role of transactive response DNA-binding protein-43 in amyotrophic lateral sclerosis and frontotemporal dementia. Curr. Opin. Neurol. 21:693–700. https://doi.org/10.1097/wco.0b013e3283168d1d.
18. Igaz, L. M., L. K. Kwong, . , V. M. Y. Lee. 2008. Enrichment of C-terminal fragments in TAR DNA-binding protein-43 cytoplasmic inclusions in brain but not in spinal cord of frontotemporal lobar degeneration and amyotrophic lateral sclerosis. Am. J. Pathol. 173:182–194. https://doi.org/10.2353/ajpath.2008.080003.
19. Neumann, M., D. M. Sampathu, . , V. M. Y. Lee. 2006. Ubiquitinated TDP-43 in frontotemporal lobar degeneration and amyotrophic lateral sclerosis. Science. 314:130–133. https://doi.org/10.1126/science.1134108.
20. Zhang, Y.-J., Y.-F. Xu, . , L. Petrucelli. 2009. Aberrant cleavage of TDP-43 enhances aggregation and cellular toxicity. Proc. Natl. Acad. Sci. U S A. 106:7607–7612. https://doi.org/10.1073/pnas.0900688106.
21. Xiao, S., T. Sanelli, . , J. Robertson. 2015. Low molecular weight species of TDP-43 generated by abnormal splicing form inclusions in amyotrophic lateral sclerosis and result in motor neuron death. Acta Neuropathol. 130:49–61. https://doi.org/10.1007/s00401-015-1412-5.
22. Igaz, L. M., L. K. Kwong, . , V. M. Y. Lee. 2009. Expression of TDP-43 C-terminal fragments in vitro recapitulates pathological features of TDP-43 proteinopathies. J. Biol. Chem. 284:8516–8524. https://doi.org/10.1074/jbc.m809462200.
23. Nunes, C., I. Mestre, . , C. Nóbrega. 2019. MSGP: the first database of the protein components of the mammalian stress granules. Database. 2019:baz031.
24. Wang, J., J.-M. Choi, . , A. A. Hyman. 2018. A molecular grammar governing the driving forces for phase separation of prion-like RNA binding proteins. Cell. 174:688–699.e16. https://doi.org/10.1016/j.cell.2018.06.006.
25. Sama, R. R. K., C. L. Ward, . , D. A. Bosco. 2013. FUS/TLS assembles into stress granules and is a prosurvival factor during hyperosmolar stress. J. Cell. Physiol. 228:2222–2231. https://doi.org/10.1002/jcp.24395.
26. Gilks, N., N. Kedersha, . , P. Anderson. 2004. Stress granule assembly is mediated by prion-like aggregation of TIA-1. Mol. Biol. Cell. 15:5383–5398. https://doi.org/10.1091/mbc.e04-08-0715.
27. He, Z., and A. Bateman. 2003. Progranulin (granulin-epithelin precursor, PC-cell-derived growth factor, acrogranin) mediates tissue repair and tumorigenesis. J. Mol. Med. 81:600–612. https://doi.org/10.1007/s00109-003-0474-3.
28. Jian, J., J. Konopka, and C. Liu. 2013. Insights into the role of progranulin in immunity, infection, and inflammation. J. Leukoc. Biol. 93:199–208. https://doi.org/10.1189/jlb.0812429.
29. Van Damme, P., A. Van Hoecke, . , W. Robberecht. 2008. Progranulin functions as a neurotrophic factor to regulate neurite outgrowth and enhance neuronal survival. J. Cell Biol. 181:37–41. https://doi.org/10.1083/jcb.200712039.
30. Elia, L. P., A. R. Mason, ., S. Finkbeiner. 2019. Genetic regulation of neuronal progranulin reveals a critical role for the autophagy-lysosome pathway. J. Neurosci. 39:3332–3344. https://doi.org/10.1523/JNEUROSCI.3498-17.2019.
31. Tanaka, Y., G. Suzuki, . , M. Nishihara. 2017. Progranulin regulates lysosomal function and biogenesis through acidification of lysosomes. Hum. Mol. Genet. 26. . ddx011–988. https://doi.org/10.1093/hmg/ddx011.
32. Gao, X., A. P. Joselin, . , J. Y. Wu. 2010. Progranulin promotes neurite outgrowth and neuronal differentiation by regulating GSK-3b. Protein Cell. 1:552–562. https://doi.org/10.1007/s13238-010-0067-1.
33. He, Z., and A. Bateman. 1999. Progranulin gene expression regulates epithelial cell growth and promotes tumor growth in vivo. Cancer Res. 59:3222–3229.
34. Ryan, C. L., D. C. Baranowski, . , A. Bateman. 2009. Progranulin is expressed within motor neurons and promotes neuronal cell survival. BMC Neurosci. 10:130. https://doi.org/10.1186/1471-2202-10-130.
35. Gass, J., W. C. Lee, . , L. Petrucelli. 2012. Progranulin regulates neuronal outgrowth independent of sortilin. Mol. Neurodegener. 7:33. https://doi.org/10.1186/1750-1326-7-33.
36. van der Zee, J., I. Le Ber, . , C. Van Broeckhoven. 2007. Mutations other than null mutations producing a pathogenic loss of progranulin in frontotemporal dementia. Hum. Mutat. 28:416. https://doi.org/10.1002/humu.9484.
37. Chow, T. W., B. L. Miller, . , D. H. Geschwind. 1999. Inheritance of frontotemporal dementia. Arch. Neurol. 56:817–822. https://doi.org/10.1001/archneur.56.7.817.
38. Arrant, A. E., V. C. Onyilo, . , E. D. Roberson. 2018. Progranulin gene therapy improves lysosomal dysfunction and microglial pathology associated with frontotemporal dementia and neuronal ceroid lipofuscinosis. J. Neurosci. 38:2341–2358. https://doi.org/10.1523/jneurosci.3081-17.2018.
39. Ward, M. E., R. Chen, . , A. J. Green. 2017. Individuals with progranulin haploinsufficiency exhibit features of neuronal ceroid lipofuscinosis. Sci. Transl Med. 9:eaah5642. https://doi.org/10.1126/scitranslmed.aah5642.
40. Mackenzie, I. R. A., D. G. Munoz, . , M. Neumann. 2011. Distinct pathological subtypes of FTLD-FUS. Acta Neuropathol. 121:207–218. https://doi.org/10.1007/s00401-010-0764-0.
41. Chitramuthu, B. P., H. P. J. Bennett, and A. Bateman. 2017. Progranulin: a new avenue towards the understanding and treatment of neurodegenerative disease. Brain. 140:3081–3104. https://doi.org/10.1093/brain/awx198.
42. Zhu, J., C. Nathan, . , A. Ding. 2002. Conversion of proepithelin to epithelins. Cell. 111:867–878. https://doi.org/10.1016/s0092-8674(02)01141-8.
43. Lee, C. W., J. N. Stankowski, . , L. Petrucelli. 2017. The lysosomal protein cathepsin L is a progranulin protease. Mol. Neurodegener. 12:55. https://doi.org/10.1186/s13024-017-0196-6.

44. Root, J., P. Merino, . , T. Kukar. 2021. Lysosome dysfunction as a cause of neurodegenerative diseases: lessons from frontotemporal dementia and amyotrophic lateral sclerosis. Neurobiol. Dis. 154:105360. https://doi.org/10.1016/j.nbd.2021.105360.

45. Holler, C. J., G. Taylor, . , T. Kukar. 2017. Intracellular proteolysis of progranulin generates stable, lysosomal granulins that are haploinsufficient in patients with frontotemporal dementia caused by GRN mutations. eNeuro. 4. . ENEURO.0100:17.2017. https://doi.org/10.1523/eneuro.0100-17.2017.

46. Shoyab, M., V. L. McDonald, . , G. D. Plowman. 1990. Epithelins 1 and 2: isolation and characterization of two cysteine-rich growth-modulating proteins. Proc. Natl. Acad. Sci. U S A. 87:7912–7916. https://doi.org/10.1073/pnas.87.20.7912.

47. Park, B., L. Buti, . , H. L. Ploegh. 2011. Granulin is a soluble cofactor for toll-like receptor 9 signaling. Immunity. 34:505–513. https://doi.org/10.1016/j.immuni.2011.01.018.

48. Ungurs, M. J., N. J. Sinden, and R. A. Stockley. 2014. Progranulin is a substrate for neutrophil-elastase and proteinase-3 in the airway and its concentration correlates with mediators of airway inflammation in COPD. Am. J. Physiol. Lung Cell Mol. Physiol. 306:L80–L87. https://doi.org/10.1152/ajplung.00221.2013.

49. Salazar, D. A., V. J. Butler, . , A. W. Kao. 2015. The progranulin cleavage products, granulins, exacerbate TDP-43 toxicity and increase TDP-43 levels. J. Neurosci. 35:9315–9328. https://doi.org/10.1523/jneurosci.4808-14.2015.

50. Bhopatkar, A. A., V. N. Uversky, and V. Rangachari. 2020. Granulins modulate liquid-liquid phase separation and aggregation of the prion-like C-terminal domain of the neurodegeneration-associated protein TDP-43. J. Biol. Chem. 295:2506–2519. https://doi.org/10.1074/jbc.ra119.011501.

51. Mao, Q., D. Wang, . , E. H. Bigio. 2017. Disease and region specificity of granulin immunopositivities in Alzheimer disease and frontotemporal lobar degeneration. J. Neuropathol. Exp. Neurol. 76:957–968. https://doi.org/10.1093/jnen/nlx085.

52. Correia, A. S., P. Patel, . , J.-P. Julien. 2015. Inflammation induces TDP-43 mislocalization and aggregation. PloS one. 10:e0140248. https://doi.org/10.1371/journal.pone.0140248.

53. Wang, H. K., Y. C. Lee, . , K. J. Tsai. 2015. Traumatic brain injury causes frontotemporal dementia and TDP-43 proteolysis. Neuroscience. 300:94–103. https://doi.org/10.1016/j.neuroscience.2015.05.013.

54. Conicella, A. E., G. H. Zerze, . , N. L. Fawzi. 2016. ALS mutations disrupt phase separation mediated by a-helical structure in the TDP-43 low-complexity C-terminal domain. Structure. 24:1537–1549. https://doi.org/10.1016/j.str.2016.07.007.

55. Ghag, G., C. J. Holler, . , V. Rangachari. 2017. Disulfide bonds and disorder in granulin-3: an unusual handshake between structural stability and plasticity. Protein Sci. 26:1759–1772. https://doi.org/10.1002/pro.3212.

56. Dean, D. N., P. Rana, . , V. Rangachari. 2018. Propagation of an ab dodecamer strain involves a three-step mechanism and a key intermediate. Biophys. J. 114:539–549. https://doi.org/10.1016/j.bpj.2017.11.3778.

57. Buell, A. K., C. Galvagnion, . , C. M. Dobson. 2014. Solution conditions determine the relative importance of nucleation and growth processes in a-synuclein aggregation. Proc. Natl. Acad. Sci. U S A. 111:7671–7676. https://doi.org/10.1073/pnas.1315346111.

58. Bhopatkar, A. A., and V. Rangachari. 2021. Are granulins copper sequestering proteins? Proteins. 89:450–461. https://doi.org/10.1002/prot.26031.

59. Dean, D. N., P. K. Das, . , V. Rangachari. 2017. Strain-specific fibril propagation by an Ab dodecamer. Sci. Rep. 7:40787–40813. https://doi.org/10.1038/srep40787.

60. Dhakal, S., C. E. Wyant, . , V. Rangachari. 2021. Prion-like C-terminal domain of TDP-43 and a-Synuclein interact synergistically to generate neurotoxic hybrid fibrils. J. Mol. Biol. 433:166953. https://doi.org/10.1016/j.jmb.2021.166953.

61. Erdős, G., and Z. Dosztányi. 2020. Analyzing protein disorder with IUPred2A. Curr. Protoc. Bioinformatics. 70:e99. https://doi.org/10.1002/cpbi.99.

62. Meszáros, B., G. Erdos, and Z. Dosztányi. 2018. IUPred2A: context-dependent prediction of protein disorder as a function of redox state and protein binding. Nucleic Acids Res. 46. . W329–w337. https://doi.org/10.1093/nar/gky384.

63. Holehouse, A. S., R. K. Das, . , R. V. Pappu. 2017. CIDER: Resources to analyze sequence-ensemble relationships of intrinsically disordered proteins. Biophys. J. 112:16–21. https://doi.org/10.1016/j.bpj.2016.11.3200.

64. Hoque, M., M. B. Mathews, and T. Pe'ery. 2010. Progranulin (granulin/epithelin precursor) and its constituent granulin repeats repress transcription from cellular promoters. J. Cell Physiol. 223:224–233. https://doi.org/10.1002/jcp.22031.

65. Plowman, G. D., J. M. Green, . , M. Shoyab. 1992. The epithelin precursor encodes two proteins with opposing activities on epithelial cell growth. J. Biol. Chem. 267:13073–13078. https://doi.org/10.1016/s0021-9258(18)42382-4.

66. Kedersha, N., M. R. Cho, . , P. Anderson. 2000. Dynamic shuttling of TIA-1 accompanies the recruitment of mRNA to mammalian stress granules. J. Cell Biol. 151:1257–1268. https://doi.org/10.1083/jcb.151.6.1257.

67. Gasset-Rosa, F., S. Lu, . , D. W. Cleveland. 2019. Cytoplasmic TDP-43 de-mixing independent of stress granules drives inhibition of nuclear import, loss of nuclear TDP-43, and cell death. Neuron. 102:339–357.e7. https://doi.org/10.1016/j.neuron.2019.02.038.

68. Wheeler, J. R., T. Matheny, . , R. Parker. 2016. Distinct stages in stress granule assembly and disassembly. eLife. 5:e18413. https://doi.org/10.7554/elife.18413.

69. Wang, C., Y. Duan, . , Y. Fang. 2020. Stress induces dynamic, cytotoxicity-antagonizing TDP-43 nuclear bodies via paraspeckle LncRNA NEAT1-mediated liquid-liquid phase separation. Mol. Cell. 79:443–458.e7. https://doi.org/10.1016/j.molcel.2020.06.019.

70. Fang, M. Y., S. Markmiller, . , G. W. Yeo. 2019. Small-molecule modulation of TDP-43 recruitment to stress granules prevents persistent TDP-43 accumulation in ALS/FTD. Neuron. 103:802–819.e11. https://doi.org/10.1016/j.neuron.2019.05.048.

71. Ciryam, P., I. A. Lambert-Smith, . , J. J. Yerbury. 2017. Spinal motor neuron protein supersaturation patterns are associated with inclusion body formation in ALS. Proc. Natl. Acad. Sci. U S A. 114:E3935. https://doi.org/10.1073/pnas.1613854114.

72. Watanabe, S., H. Inami, . , K. Yamanaka. 2020. Aggresome formation and liquid–liquid phase separation independently induce cytoplasmic aggregation of TAR DNA-binding protein 43. Cell Death Dis. 11:909. https://doi.org/10.1038/s41419-020-03116-2.

73. Choi, J.-M., A. S. Holehouse, and R. V. Pappu. 2020. Physical principles underlying the complex biology of intracellular phase transitions. Annu. Rev. Biophys. 49:107–133. https://doi.org/10.1146/annurev-biophys-121219-081629.

74. Choi, J.-M., F. Dar, and R. V. Pappu. 2019. LASSI: a lattice model for simulating phase transitions of multivalent proteins. PLOS Comput. Biol. 15:e1007028. https://doi.org/10.1371/journal.pcbi.1007028.

75. Murthy, A. C., W. S. Tang, . , N. L. Fawzi. 2021. Molecular interactions contributing to FUS SYGQ LC-RGG phase separation and co-partitioning with RNA polymerase II heptads. Nat. Struct. Mol. Biol. 28:923–935. https://doi.org/10.1038/s41594-021-00677-4.

76. Pak, C. W., M. Kosno, . , M. K. Rosen. 2016. Sequence determinants of intracellular phase separation by complex coacervation of a disordered protein. Mol. Cell. 63:72–85. https://doi.org/10.1016/j.molcel.2016.05.042.

77. Li, H.-R., W.-C. Chiang, . , J.-R. Huang. 2018. TAR DNA-binding protein 43 (TDP-43) liquid-liquid phase separation is mediated by just a few aromatic residues. J. Biol. Chem. 293:6090–6098. https://doi.org/10.1074/jbc.ac117.001037.

78. Babinchak, W. M., B. K. Dumm, . , W. K. Surewicz. 2020. Small molecules as potent biphasic modulators of protein liquid-liquid

phase separation. Nat. Commun. 11:5574. https://doi.org/10.1038/s41467-020-19211-z.

79. Schmidt, H. B., and R. Rohatgi. 2016. In vivo formation of vacuolated multi-phase compartments lacking membranes. Cell Rep. 16:1228–1236. https://doi.org/10.1016/j.celrep.2016.06.088.
80. Wang, A., A. E. Conicella, . , N. L. Fawzi. 2018. A single N-terminal phosphomimic disrupts TDP-43 polymerization, phase separation, and RNA splicing. EMBO J. 37:e97452. https://doi.org/10.15252/embj.201797452.
81. Lim, L., Y. Wei, . , J. Song. 2016. ALS-causing mutations significantly perturb the self-assembly and interaction with nucleic acid of the intrinsically disordered prion-like domain of TDP-43. PLoS Biol. 14:e1002338. https://doi.org/10.1371/journal.pbio.1002338.
82. Uversky, V. N. 2017. Protein intrinsic disorder-based liquid–liquid phase transitions in biological systems: complex coacervates and membrane-less organelles. Adv. Colloid Interf. Sci. 239:97–114. https://doi.org/10.1016/j.cis.2016.05.012.
83. Muiznieks, L. D., S. Sharpe, . , F. W. Keeley. 2018. Role of liquid–liquid phase separation in assembly of elastin and other extracellular matrix proteins. J. Mol. Biol. 430:4741–4753. https://doi.org/10.1016/j.jmb.2018.06.010.
84. Majumdar, A., P. Dogra, . , S. Mukhopadhyay. 2019. Liquid–liquid phase separation is driven by large-scale conformational unwinding and fluctuations of intrinsically disordered protein molecules. J. Phys. Chem. Lett. 10:3929–3936. https://doi.org/10.1021/acs.jpclett.9b01731.
85. Brangwynne, C. P., P. Tompa, and R. V. Pappu. 2015. Polymer physics of intracellular phase transitions. Nat. Phys. 11:899–904. https://doi.org/10.1038/nphys3532.
86. Wright, P. E., and H. J. Dyson. 2015. Intrinsically disordered proteins in cellular signalling and regulation. Nat. Rev. Mol. Cell Biol. 16:18– 29. https://doi.org/10.1038/nrm3920.
87. Düster, R., I. H. Kaltheuner, . , M. Geyer. 2021. 1,6-Hexanediol, commonly used to dissolve liquid–liquid phase separated condensates, directly impairs kinase and phosphatase activities. J. Biol. Chem. 296:100260.
88. Shulga, N., and D. S. Goldfarb. 2003. Binding dynamics of structural nucleoporins govern nuclear pore complex permeability and may mediate channel gating. Mol. Cell Biol. 23:534–542. https://doi.org/10.1128/mcb.23.2.534-542.2003.
89. Pantoja-Uceda, D., C. Stuani, . , M. Mompeán. 2021. Phe-Gly motifs drive fibrillization of TDP-43's prion-like domain condensates. PLoS Biol. 19:e3001198. https://doi.org/10.1371/journal.pbio.3001198.
90. Li, H. R., T. C. Chen, . , J. R. Huang. 2018. The physical forces mediating self-association and phase-separation in the C-terminal domain of TDP-43. Biochim. Biophys. Acta Proteins Proteom. 1866:214–223. https://doi.org/10.1016/j.bbapap.2017.10.001.
91. López-Mirabal, H. R., and J. R. Winther. 2008. Redox characteristics of the eukaryotic cytosol. Biochim. Biophys. Acta. 1783:629–640. https://doi.org/10.1016/j.bbamcr.2007.10.013.
92. Xue, C., T. Y. Lin, . , Z. Guo. 2017. Thioflavin T as an amyloid dye: fibril quantification, optimal concentration and effect on aggregation. R. Soc. Open Sci. 4:160696. https://doi.org/10.1098/rsos.160696.
93. Kaur, T., M. Raju, . , P. R. Banerjee. 2021. Sequence-encoded and composition-dependent protein-RNA interactions control multiphasic condensate morphologies. Nat. Commun. 12:872. https://doi.org/10.1038/s41467-021-21089-4.
94. Bateman, A., D. Belcourt, . , S. Solomon. 1990. Granulins, a novel class of peptide from leukocytes. Biochem. Biophys. Res. Commun. 173:1161–1168. https://doi.org/10.1016/s0006-291x(05)80908-8.
95. Bateman, A., and H. P. Bennett. 1998. Granulins: the structure and function of an emerging family of growth factors. J. Endocrinol. 158:145–151. https://doi.org/10.1677/joe.0.1580145.
96. Horinokita, I., H. Hayashi, . , N. Takagi. 2019. Involvement of progranulin and granulin expression in inflammatory responses after cerebral ischemia. Int. J. Mol. Sci. 20:5210. https://doi.org/10.3390/ijms20205210.
97. Kao, A. W., A. McKay, . , E. J. Huang. 2017. Progranulin, lysosomal regulation and neurodegenerative disease. Nat. Rev. Neurosci. 18:325–333. https://doi.org/10.1038/nrn.2017.36.
98. Hu, F., T. Padukkavidana, . , S. M. Strittmatter. 2010. Sortilin-mediated endocytosis determines levels of the frontotemporal dementia protein, progranulin. Neuron. 68:654–667. https://doi.org/10.1016/j.neuron.2010.09.034.
99. Feneberg, E., P. D. Charles, . , M. R. Turner. 2020. Detection and quantification of novel C-terminal TDP-43 fragments in ALS-TDP. Brain Pathol. 31:e12923. https://doi.org/10.1111/bpa.12923.
100. Babinchak, W. M., R. Haider, . , W. K. Surewicz. 2019. The role of liquid-liquid phase separation in aggregation of the TDP-43 low-complexity domain. J. Biol. Chem. 294:6306–6317. https://doi.org/10.1074/jbc.ra118.007222.
101. Mompeán, M., A. Chakrabartty, . , D. V. Laurents. 2016. Electrostatic repulsion governs TDP-43 C-terminal domain aggregation. PLOS Biol. 14:e1002447. https://doi.org/10.1371/journal.pbio.1002447.
102. Ruff, K. M., F. Dar, and R. V. Pappu. 2021. Ligand effects on phase separation of multivalent macromolecules. Proc. Natl. Acad. Sci. U S A. 118. . e2017184118. https://doi.org/10.1073/pnas.2017184118.
103. Zhang, T., H. Du, . , F. Hu. 2021. Differential regulation of progranulin derived granulin peptides. Preprint at bioRxiv. https://doi.org/10.1101/2021.01.08.425959.
104. Mazmanian, K., K. Sargsyan, . , C. Lim. 2016. Preferred hydrogen-bonding partners of cysteine: implications for regulating cys functions. J. Phys. Chem. B. 120:10288–10296. https://doi.org/10.1021/acs.jpcb.6b08109.
105. Yang, P., C. Mathieu, . , J. P. Taylor. 2020. G3BP1 is a tunable switch that triggers phase separation to assemble stress granules. Cell. 181:325–345.e28. https://doi.org/10.1016/j.cell.2020.03.046.
106. Guil, S., J. C. Long, and J. F. Caćeres. 2006. hnRNP A1 relocalization to the stress granules reflects a role in the stress response. Mol. Cell Biol. 26:5744–5758. https://doi.org/10.1128/mcb.00224-06.
107. Malaspina, A., N. Kaushik, and J. de Belleroche. 2008. Differential expression of 14 genes in amyotrophic lateral sclerosis spinal cord detected using gridded cDNA arrays. J. Neurochem. 77:132–145. https://doi.org/10.1046/j.1471-4159.2001.00231.x.
108. Baker, C. A., and L. Manuelidis. 2003. Unique inflammatory RNA profiles of microglia in Creutzfeldt-Jakob disease. Proc. Natl. Acad. Sci. U S A. 100:675–679. https://doi.org/10.1073/pnas.0237313100.
109. Ahmed, Z., I. R. Mackenzie, . , D. W. Dickson. 2007. Progranulin in frontotemporal lobar degeneration and neuroinflammation. J. Neuroinflammation. 4:7. https://doi.org/10.1186/1742-2094-4-7.